ACS Photonics

Caltech Library

Subscriber access provided by Caltech Library

Article

Energy Transport State Resolved Raman for Probing Interface Energy Transport and Hot Carrier Diffusion in Few-Layered MoS

Pengyu Yuan, Ridong Wang, Hong Tan, Tianyu Wang, and Xinwei Wang

ACS Photonics, **Just Accepted Manuscript** • DOI: 10.1021/acsphotonics.7b00815 • Publication Date (Web): 12 Sep 2017

Downloaded from http://pubs.acs.org on September 16, 2017

Just Accepted

"Just Accepted" manuscripts have been peer-reviewed and accepted for publication. They are posted online prior to technical editing, formatting for publication and author proofing. The American Chemical Society provides "Just Accepted" as a free service to the research community to expedite the dissemination of scientific material as soon as possible after acceptance. "Just Accepted" manuscripts appear in full in PDF format accompanied by an HTML abstract. "Just Accepted" manuscripts have been fully peer reviewed, but should not be considered the official version of record. They are accessible to all readers and citable by the Digital Object Identifier (DOI®). "Just Accepted" is an optional service offered to authors. Therefore, the "Just Accepted" Web site may not include all articles that will be published in the journal. After a manuscript is technically edited and formatted, it will be removed from the "Just Accepted" Web site and published as an ASAP article. Note that technical editing may introduce minor changes to the manuscript text and/or graphics which could affect content, and all legal disclaimers and ethical guidelines that apply to the journal pertain. ACS cannot be held responsible for errors or consequences arising from the use of information contained in these "Just Accepted" manuscripts.

ACS Publications

ACS Photonics is published by the American Chemical Society. 1155 Sixteenth Street N.W., Washington, DC 20036

Published by American Chemical Society. Copyright © American Chemical Society. However, no copyright claim is made to original U.S. Government works, or works produced by employees of any Commonwealth realm Crown government in the course of their duties.

1
2
3
4
5
6
7
8
9
10
11
12
13
14
15
16
17
18
19
20
21
22
23
24
25
26
27
28
29
30
31
32
33
34
35
36
37
38
39
40
41
42
43
44
45
46
47
48
49
50
51
52
53
54
55
56
57
58
59
60

Energy Transport State Resolved Raman for Probing Interface Energy Transport and Hot Carrier Diffusion in Few-Layered MoS_2

Pengyu Yuan[1, ‡], Ridong Wang[1, ‡], Hong Tan[2], Tianyu Wang[1], Xinwei Wang[1,*]

[1] Department of Mechanical Engineering, Iowa State University, Ames, IA 50011, USA.

[2] School of Energy and Power Engineering, Nanjing University of Science and Technology, Nanjing, Jiangsu 210094, China.

‡: Equal contribution authors.

*E-mail: xwang3@iastate.edu

Abstract

Quantitative understanding of 2D atomic layer interface thermal resistance (R) based on Raman characterization is significantly hindered by unknown sample-to-sample optical properties variation, interface-induced optical interference, off-normal laser irradiation, and large thermal-Raman calibration uncertainties. In this work, we develop a novel energy transport state resolved Raman (ET-Raman) to resolve these critical issues, and also consider the hot carrier diffusion, which is crucial but has been rarely considered during interface energy transport study. In ET-Raman, by constructing two steady heat conduction states with different laser spot sizes, we differentiate the effect of R and hot carrier diffusion coefficient (D). By constructing an extreme state of zero/negligible heat conduction using a picosecond laser, we differentiate the effect of R and material's specific heat. In the end, we precisely determine R and D without need of laser absorption and temperature rise of the 2D atomic layer. Seven MoS_2 samples (6.6~17.4 nm) on

c-Si are characterized using ET-Raman. Their *D* is measured in the order of 1.0 cm^2/s, increasing against the MoS_2 thickness. This is attributed to the weaker in-plane electron-phonon interaction in thicker samples, enhanced screening of long-range disorder, and improved charge impurities mitigation. *R* is determined as 1.22~1.87×10^{-7} $K\cdot m^2/W$, decreasing with the MoS_2 thickness. This is explained by the interface spacing variation due to thermal expansion mismatch between MoS_2 and Si, and increased stiffness of thicker MoS_2. The local interface spacing is uncovered by comparing the theoretical Raman intensity and experimental data, and is correlated with the observed *R* variation.

Keywords: hot carrier diffusion, interface thermal resistance, 2D atomic layer, Raman spectroscopy, picosecond laser, energy transport state design

1
2
3
4
5
6
7
8
9
10
11
12
13
14
15
16
17
18
19
20
21
22
23
24
25
26
27
28
29
30
31
32
33
34
35
36
37
38
39
40
41
42
43
44
45
46
47
48
49
50
51
52
53
54
55
56
57
58
59
60

The bottleneck of most modern technologies and energy solutions has been attributed to the thermal problems at the nanoscale.[1-2] Especially, the thermal transport across interfaces can significantly influence the overall performance of nanosystems, such as microelectronics, photonics, and thermoelectric devices. The direct effect on device performance is that the high interface thermal resistance could cause electronic functionality catastrophic failures of nano-devices.[3] So accurate thermal-physical characterization of the 2D interface is very important for both fundamental research and industrial applications. However, the measurement of interface energy coupling is very challenging and complicated because interface thermal conductance is related to the characteristics of the interface properties, such as the effect of roughness, disorder, dislocations, and bonding, *etc*.[4]

Besides, as has been studied in 2D semiconductor materials, the electrically and optically generated hot carriers can strongly contribute to the thermal diffusion and heat dissipation in electronic devices.[5] For example, when scaling down the devices, the hot carrier could also induce the degradation of MOSFETs which will cause time-dependent shift in the measured devices parameters.[6] For photo-detection and photovoltaics devices, thermalization of the light-induced hot carrier contributes to most of the efficiency loss.[7] The transport of hot carriers, like free electrons in metals, is dominated by various interactions between carriers and other elementary excitations in semiconductor materials.[8] Therefore, the study of hot carrier transport could provide us deep insight about the scattering process and energy distribution in semiconductors.

To date, several approaches have been applied to study the interface thermal transport between 2D material and its substrate either by experiment or theoretical simulation. Some well-known experiment techniques include the 3ω method,[9] thermoreflectance method including both time-

domain and frequency-domain analysis,[10] and Raman based thermal probing method.[11-12] For theoretical methods, molecular dynamics (MD) simulation[13] and acoustic/diffuse mismatch model[14] are widely used. Remarkably, for using Raman-based techniques, the hot carrier diffusion effect on thermal transport has not been carefully taken into account before. This usually leads to an underestimated heating area because the hot carrier diffusion could significantly extend the heating size. As a result, an overestimated laser heating flux could lead to less accurate thermal properties evaluation (*e.g.,* underestimated interface thermal resistance). On the other hand, for the hot carrier diffusion study, the most common and straight forward approach is to apply a voltage to the electric contact to control the electron population in the material. Unfortunately, there is still a concern that the electrical contacts may cause screening disorder in field-effect transistors.[15] Thus, optical-based measurements are believed to provide the intrinsic hot carrier transport properties of the material. To this end, several optical techniques including transient grating,[16] photoluminescence (including both time-of-flight configuration[17] and the spatially resolved geometry[18]), and spatially and temporally resolved pump-probe techniques[19-20] have been used to study the hot carrier diffusion. These techniques allow us to directly observe the expansion of the carrier density profile so that any changes in the diffusion coefficient caused by carrier or lattice temperature could be studied simultaneously. However, most of these work are focused on graphene,[21] reduced graphene oxide,[22-23] CdSe,[16] *etc*. For the promising semiconductor materials-transition metal dichalcogenides (TMDs), less work has been reported so far.

For the optical-based measurement of both interface thermal resistance (R) and carrier diffusion coefficient, the optical properties [the refractive index (n) and extinction coefficient (k_L)] of the samples are the must-know parameters. They are related to the interaction between a material

1
2
3
4
5
6
7
8
9
10
11
12
13
14
15
16
17
18
19
20
21
22
23
24
25
26
27
28
29
30
31
32
33
34
35
36
37
38
39
40
41
42
43
44
45
46
47
48
49
50
51
52
53
54
55
56
57
58
59
60

and incident light and vary a lot from sample to sample. Especially, for real 2D interface structure (*e.g.* MoS_2 nanosheets on SiO_2 substrate), a tiny change of the local spacing can significantly change the laser optical absorption, leading to large measurement errors.[24] Additionally, like the Raman-based techniques developed by Cai *et al.*[25] and Judek *et al.*[26] to explore the 2D interface thermal transport properties, the laser absorption coefficient can only be estimated based on others' work rather than direct measurement, which could introduce great and yet unevaluated errors. The measured n and k_L values also vary a lot from different methods. For example, at 532 nm wavelength, the refractive index of MoS_2 is ~3.05 determined by spectroscopic ellipsometry[27] and ~5.2 (1.7 times larger) by a spatially resolved spectrum system[28].

In our recently published work, we have developed a new technique and systemically studied the hot carrier diffusion effect on thermal transport. R and D are simultaneously determined for four sub-10 nm thick virgin MoS_2 on c-Si.[5] In this work, we make another breakthrough on the basis of that technique and develop a novel and more advanced technique: energy transport state-resolved Raman (ET-Raman) to study the 2D materials' thermal response under different laser heating states. By this technique, we could also determine R and D but completely eliminate the large errors introduced by laser absorption evaluation and Raman property temperature coefficient calibration. These two factors significantly affect the measurement reported in literatures and are responsible for the very large reported data deviation. Our ET-Raman is based on two extreme energy transport situations: zero-transport using a picosecond (ps) laser Raman and steady-state using a continuous-wave (CW) laser Raman. One of the most attractive perspectives is that we do not need to know the laser absorption coefficient or the temperature coefficients of the Raman properties. D and R could be determined by just comparing the Raman

wavenumber shift measured from different energy transport states (in time and space domains). So this technique is believed to eliminate the errors brought in by local optical absorption evaluation, temperature coefficient calibration, and the effects from electrical contact. Therefore it provides a far more accurate understanding of interface energy coupling and hot carrier diffusion. This technique is successfully applied here to determine *D* and *R* of seven few-layered MoS_2 samples on c-Si substrate. The thickness of MoS_2 nanosheets ranges from 6.6 nm to 17.4 nm in this work.

Results and Discussions:

Physical Model of Energy Transport State-resolved Raman (ET-Raman)

In the ET-Raman technique, we construct three distinct energy transport states in both space and time domains, and probe the materials' thermal response. Figure 1 (a) shows the physical principles of this technique. A laser with 532 nm (E=2.33 eV) wavelength irradiates the MoS_2 sample for both laser heating and Raman probe. Because the excitation energy E is greater than the band gap of MoS_2 (E_g=1.29~1.80 eV), the absorbed photons will excite the electrons (e) to the conduction band with holes (h) left in the valence band. This excitation results in the formation of hot electrons and holes (hot carriers) because they have higher energies compared to the Fermi Energy. Then the hot carriers will lose part of the photon energy ΔE=(E-E_g) via direct phonon emission and indirect cooling through collisions with other electrons by a rapid non-radiative process, on a time scale of 0.1 ps.[29] This happens so quickly that the carrier diffusion during this process will not be included in this work. The hot electrons will store the rest part of photon energy (E_g) and diffuse out of the excitation spot before recombining with holes. This diffusion will result in a significantly wider thermal source spatial redistribution in

1
2
3
4
5
6
7
8
9
10
11
12
13
14
15
16
17
18
19
20
21
22
23
24
25
26
27
28
29
30
31
32
33
34
35
36
37
38
39
40
41
42
43
44
45
46
47
48
49
50
51
52
53
54
55
56
57
58
59
60

the sample. The excited electrons and holes move together as *e-h* pairs in this diffusion process due to the Coulomb attraction. It typically takes nanoseconds for this diffusion process so we have to consider the diffusion effect.[30] Since few-layered MoS_2 has an indirect bandgap, the crystal momentum conservation could strongly restrict the radiative recombination of carriers. As a result, the excited hot electrons would release the laser energy via non-radiative recombination with holes by exciting phonons. The energy of these phonons in MoS_2 nanosheets dissipates within the sample and through the interface down to the substrate to raise the local temperature. The phonons eventually reach thermal equilibrium with the electrons.

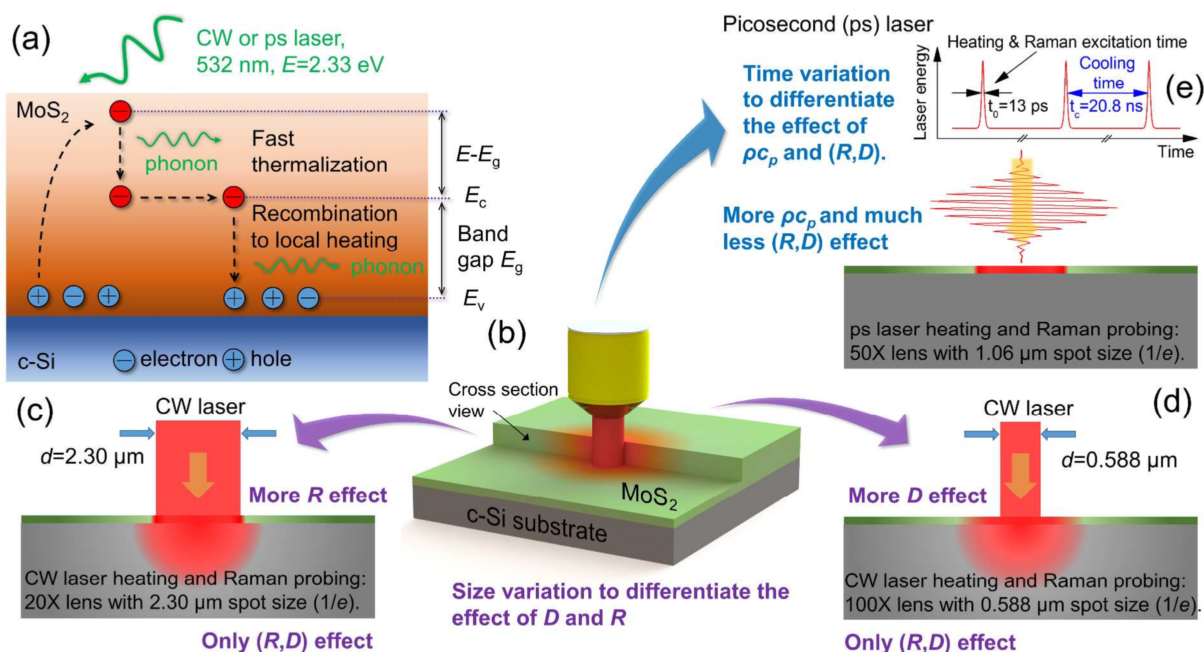

Figure 1. (a) Physical model of hot carrier generation, diffusion, and recombination in MoS_2 under laser illumination (not to scale). The photons generate hot carriers in the MoS_2 sample by exciting electrons (*e*) to the conduction band (E_c), leaving holes (*h*) in the valance band (E_v). The hot carriers transfer part of the photon energy (E-E_g) to the lattice in the form of thermal energy by fast thermalization (femtoseconds), diffuse out of the direct laser heating region to the low

1
2
3
4
5
6
7
8
9
10
11
12
13
14
15
16
17
18
19
20
21
22
23
24
25
26
27
28
29
30
31
32
33
34
35
36
37
38
39
40
41
42
43
44
45
46
47
48
49
50
51
52
53
54
55
56
57
58
59
60

population region, and then recombine with holes to release the rest part of the photon energy (E_g) through phonon emission (carrier-phonon scattering). These hot carrier generation, diffusion, and recombination processes could strongly extend the heating area size and therefore have significant effect on the final temperature distribution. (b) An artistic illustration of the experiment concept. Examined MoS_2 nanosheets (6.6~17.4 nm thick) are placed onto the typical c-Si substrate, and a 532 nm continuous-wave (CW) laser or picosecond (ps) laser is simultaneously causing and probing the local temperature rise to generate three different energy transport states in space and time domains [(c)- (e)]. We use two objective lenses (20× and 100×) for CW laser to achieve different laser spot size heating with simultaneous Raman probing to detect the local temperature rise to study (R, D) effect. (c) Heating effect of CW laser under 20× objective. The diameter of the laser spot size is around 2.28 µm (1/e profile). (d) Under 100× objective, the diameter is smaller which is around 0.588 µm (1/e profile). (e) By using a ps laser, hot carriers do not have enough time to recombine with holes within every pulse width (13 ps). Also there is extremely small heat conduction from the heating region. As a result, the temperature rise is determined by the sample's volumetric heat capacity (ρc_p) with negligible effect from (R, D).

The first energy transport state in our technique is the steady-state heating, and it has two sub-states with different laser heating sizes. As shown in Figure 1 (c) and (d), we use a CW laser source to generate steady-state heating to study the temperature profile that depends on (R, D) effect. Moreover, by using different objectives (20× and 100×) to have the size variation, we could differentiate the effect of D and R. In Fig. 1 (c), the laser heating spot under a 20× (NA=0.4) objective has a diameter around 2.30 µm (1/e peak value). Since the MoS_2 nanosheets will absorb the laser energy, they will conduct the absorbed energy directly to substrate via R and

1
2
3
4
5
6
7
8
9
10
11
12
13
14
15
16
17
18
19
20
21
22
23
24
25
26
27
28
29
30
31
32
33
34
35
36
37
38
39
40
41
42
43
44
45
46
47
48
49
50
51
52
53
54
55
56
57
58
59
60

to the in-plane direction then to the substrate via the interface (effects of both *R* and *D*). At the same time of laser heating, the same laser beam also excites Raman signal by which we could collect to get the temperature profile of the sample. By using different laser powers (*P*), we can obtain one parameter, called Raman shift power coefficient (RSC): $\chi_{CW1}=\partial\omega/\partial P$. As expected, χ_{CW1} is determined by *R*, *D*, laser absorption coefficient, and temperature coefficient of Raman shift. Then, as shown in Fig. 1(d), we reduce the laser heating dimension to a much smaller level by a 100× (NA=0.8) objective (0.588 μm), and we also obtain RSC from this experiment as χ_{CW2}. At this steady state, the *D* of the 2D material will have more influence on the measured temperature than that under 20× objective. Therefore, these two steady states construction could differentiate the effect of *D* and *R* in the measured RSC by Raman spectroscopy. Note although we mention temperature here as they are reflected in RSC, we do not need to determine the absolute temperature rise in the whole technique.

The second energy transport state is completely opposite to the steady-state: it has zero-transport. In this experiment, we apply a ps laser under 50× (NA=0.5) objective with r_0 as 0.531 μm (1/*e* peak value) with the same wavelength as the CW laser to focus on the sample to do localized heating and Raman experiment. In the same way, we obtain the RSC for this ps laser heating case: $\chi_{ps}=\partial\omega/\partial P$. Here, we neglect the heat conduction from the heating region. Also the sample will be fully cooled to the ambient temperature during the pulse interval (see Supporting Information S1 for details). As a result, the RSC (χ_{ps}) is mainly coming from the volumetric heat capacity of the sample (ρc_p). *D* and *R* have an extremely limited contribution to the temperature rise so that we could use this heating state to distinguish the roles of ρc_p and (*R*, *D*).

In our Raman experiment, the measured RSC of both MoS_2 and c-Si are Raman-intensity weighted average of the sample. For the zero-transport state, the measured temperature rise is

also time averaged over the pulse width. Besides, we do not consider the heat loss to the environment during the Raman measurement in atmospheric condition (see Supporting Information S4 for details). All of these will be also considered in the following 3D numerical simulation for data processing.

After these three energy transport states experiments, we will define the dimensionless normalized RSC as: $\Theta_1 = \chi_{CW1}/\chi_{ps}$ and $\Theta_2 = \chi_{CW2}/\chi_{ps}$. Although χ_{CW1}, χ_{CW2}, and χ_{ps} are all influenced by the Raman temperature coefficient and the laser absorption in the sample, this normalized RSC completely rules out the effect of laser absorption and Raman temperature coefficients. Θ_1 and Θ_2 are only a function of the 2D and substrate materials' ρc_p, R, and D. Using a 3D heat conduction model to include all these properties, we could finally determine D and R of the 2D material. The whole measurement does not involve absorbed laser heating power determination and absolute temperature rise determination. This eliminates the large uncertainties brought in by these two key factors in the past measurements.

Physical model and governing equations for data processing

For the steady-state heating, the generation and diffusion of heat and electrical carriers in the sample are governed by two partial differential equations in steady state ($\partial N / \partial t = 0$).[31-32] The first one is the carrier diffusion equation to determine the carrier concentration $\Delta N(\mathrm{r},t)\,(\mathrm{cm}^{-3})$:

$$D\nabla^2 \Delta N - \frac{\Delta N}{\tau} + \frac{\partial n_0}{\partial T_{\mathrm{CW}}}\frac{\Delta T_{\mathrm{CW}}}{\tau} + \Phi\alpha = 0, \tag{1}$$

where D (cm^2/s), τ (s) and Φ (photons/cm^{3}s) are the carrier diffusion coefficient, the electron-hole recombination time of MoS_2 and the incident photon flux of the laser source. $\alpha\,(\mathrm{cm}^{-1})$ is the

optical absorption coefficient of the MoS_2 nanosheets. n_0 (cm^{-3}) is the equilibrium free-carrier density at temperature T. The first term on the left side is related to hot carrier diffusion. The second term: $\Delta N/\tau$ represents the electron-hole recombination. The thermal activation term $(\partial n_0 / \partial T_{CW})\Delta T_{CW} / \tau$ is related to the carrier creation due to temperature rise. It is negligible under the relatively low-temperature rise and in small free-carrier density case.[5, 31, 33] In our experiment, for the 6.6 nm thick sample, the temperature rise under 20× objective is estimated to be only 1.3 K/mW (χ_{CW1}=0.26 cm^{-1}/mW, and the Raman temperature coefficient is estimated from our previous work[5] as 0.20 cm^{-1}/K). Besides, the free carrier density at equilibrium could be given as $n_0 = N_s \exp(-E_g / 2k_B T)$, where N_s is the number per unit volume of effectively available states. It is in the of order 10^{19} cm^{-3} at room temperature and increases with temperature. k_B is the Boltzmann's constant. At room temperature, $k_B T$ = 0.026 eV. So $k_B T \quad E_g$(1.38 eV) gives a very small n_0 (room temperature) to neglect the thermal activation term. The last term $\Phi\alpha$ represents the carrier photogeneration source. In our work, the MoS_2 nanosheets are very thin (sub-20 nm) compared with its lateral dimension (5 ~ 12 μm), so we will neglect the hot carrier gradient in the thickness direction. Therefore, Eq. (1) only considers the in-plane direction diffusion.

The second equation is the thermal diffusion equation which involves the free carrier density since non-radiative recombination provides a second heat source:

$$k_T \nabla^2 \Delta T_{CW} + (h\nu - E_g)\Phi\alpha + \frac{E_g \Delta N}{\tau} = 0, \tag{2}$$

where $\Delta T_{CW}(\mathrm{r}, t)$ (K), k_T (W/mK) are the temperature rise in the steady state heating, the thermal conductivity of few-layered MoS_2. And hv (2.33 eV) is the photon energy of the laser source.

The second term of Eq. (2), $(h\nu - E_g)\Phi\alpha$, which is proportional to ($h\nu$–E_g), represents the heat generation due to photo-generated carriers giving off the excess energy to the MoS_2 lattice. The last term $E_g\Delta N / \tau$ contains the carrier concentration and represents the heat generation through the non-radiative recombination of free carriers.

The hot electrons will diffuse in the sample until they recombine with holes to release the energy through the non-radiative recombination transition. So the real heating area will not be merely the laser irradiating area, but will be strongly affected by the hot carrier diffusion length ($L_D = \sqrt{\tau D}$). When the laser heating spot size (radius: 0.294 μm to 1.15 μm) is comparable to, or smaller than the carrier diffusion length, this effect becomes more prominent. If the laser heating spot size is sufficiently large, the hot carrier diffusion will have less or negligible effect on the heating area. For few-layered MoS_2, the hot carrier diffusion length is in the order of 0.1 μm.[20, 34] So we could observe different heating phenomena in MoS_2 by changing the laser heating spot size. Note that we do not consider the surface recombination process due to the *p*-type Si we used in this work. Besides, because of the long diffusion length of Si (around 700 μm), the transmitted laser energy to Si only heats it by the fast thermalization process ($\Delta E = E - E_g\big|_{\text{c-Si}}$). Detailed discussions for this consideration could be found in our previous work.[5]

When we use the ps laser to generate the zero-transport heating state, the laser pulse (13 ps) is so short that only the fast thermalization process happens and we could neglect the heat conduction in the lattice here as discussed above. By only considering the laser absorption in MoS_2 sample and its substrate, we have

$$\rho c_{\text{p}} \frac{\partial \Delta T_{\text{ps}}}{\partial t} = \alpha I\left(\frac{h\nu - E_g}{h\nu}\right), \tag{3}$$

ACS Paragon Plus Environment

1
2
3
4
5
6
7
8
9
10
11
12
13
14
15
16
17
18
19
20
21
22
23
24
25
26
27
28
29
30
31
32
33
34
35
36
37
38
39
40
41
42
43
44
45
46
47
48
49
50
51
52
53
54
55
56
57
58
59
60

where I (W/cm^2) is the laser intensity, t is the time. $\Delta T_{\text{ps}}(\text{r},t)$ is the temperature rise from the zero-transport state. After considering both space and time domain Gaussian distributions, and the Beer-Lambert law, the laser intensity (heat flux) is given by:

$$I(r,z,t)=\frac{I_0}{\tau_L}\exp\left[-\frac{r^2}{r_0^2}\right]\exp\left[-\ln(2)\frac{t^2}{t_0^2}\right]\exp\left[-\frac{z}{\tau_L}\right], \quad (4)$$

where I_0 (W/cm^2) is the peak laser intensity, r_0 (0.53 μm) is the laser spot radius of ps laser, t_0 (6.5 ps) is the half pulse width. $\tau_{\text{L}}=\lambda/4\pi k_{\text{L}}$ is the laser absorption depth. λ=532 nm (the laser wavelength), and k_{L} is the extinction coefficient. So we have $\tau_{\text{L}}(MoS_2)$=38.5 nm, and τ_{L}(c-Si)=820 nm. Because the thickness of MoS_2 nanosheets (6.6 nm to 17.4 nm) is smaller than its laser absorption depth, both MoS_2 and c-Si will absorb the laser energy and be heated.

As a result, the measured temperature rise of MoS_2 is actually determined by the hot carrier diffusion coefficient and the interface thermal resistance under steady-state heating and only by laser absorption rate and ρc_{p} under zero-transport state heating. By solving Eqs. (1)-(4), we could rule out the laser absorption term and deduce the ratio of the temperature rise ($\bar{T}_{\text{CW}}/\bar{T}_{\text{ps}}$) of two materials from two heating states. The ratio is just the normalized RSC. Then we solve Eqs. (3) and (4) to analyze the experimental results and determine the R and D value. In our work, the temperature difference between MoS_2 and c-Si is determined and used. This treatment has taken into full consideration of the temperature rise effect of the c-Si substrate.

Figure 2 shows the schematic of the Raman experiment setup. (see Materials and Methods section for more details) Figure 2(b) is the structure of our MoS_2 supported on the c-Si substrate. Figure 2(c) shows the atomic structure of the typical layered MoS_2. The Mo atom is in the middle

1
2
3
4
5
6
7
8
9
10
11
12
13
14
15
16
17
18
19
20
21
22
23
24
25
26
27
28
29
30
31
32
33
34
35
36
37
38
39
40
41
42
43
44
45
46
47
48
49
50
51
52
53
54
55
56
57
58
59
60

for each layer and the distance between each layer is around 0.65 nm. Figure 2(d) is the typical Raman spectrum of two vibration modes of MoS_2 (E^1_{2g} and A_{1g}) and c-Si LO phonon mode by 532 nm laser. The E^1_{2g} mode (~383 cm^{-1}) is associated with in-plane opposite vibration of two sulfur atoms with respect to the molybdenum atom, whereas the A_{1g} mode (~408 cm^{-1}) is associated with the out-of-plane vibration of only sulfur atoms in opposite directions.[35]

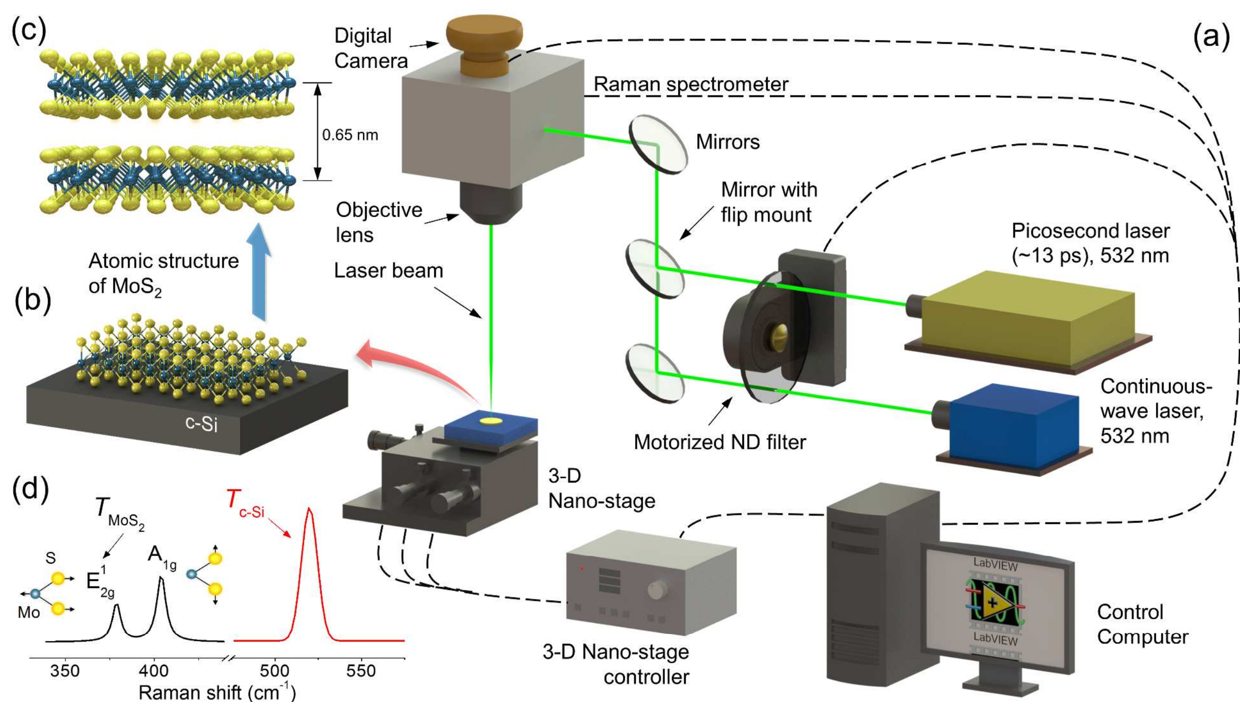

Figure 2. Schematic of the experimental setup for the micro-Raman experiment of MoS_2/c-Si sample. (a) A typical MoS_2/c-Si sample is illuminated by CW and ps 532 nm (2.33 eV) green laser. The laser source could be switched by using a flip mounted mirror. The Raman signals of MoS_2 and c-Si are excited by the same laser and collected by a confocal Raman spectrometer. The laser power is adjusted by a motorized ND filter. The spectrometer and ND filter are controlled by a LabVIEW-based software. (b) The MoS_2 nanosheets are supported on c-Si substrate. Here we use the single-layered MoS_2 to demonstrate the structure. (c) The atomic

structure of MoS_2 from a side view. The big blue balls stand for the Mo atoms, and small yellow balls are Sulphur atoms. The distance between two adjacent layers is around 0.65 nm. (d) Raman spectra of MoS_2 and c-Si are excited by the 532 nm laser in air ambient environment. Temperatures of both MoS_2 and c-Si can be determined simultaneously by their Raman spectra. E^1_{2g} (~383 cm^{-1}), A_{1g} (~408 cm^{-1}) modes, and c-Si (~519 cm^{-1}) LO phonon mode are observed in our seven samples. Here we choose the E^1_{2g} mode to evaluate the MoS_2 temperature.

Sample preparation and characterization

We prepare seven few-layered MoS_2 samples by micromechanical cleavage technique (see Material and Methods section for more details). The lateral size of layered MoS_2 nanosheets has an equivalent radius ranging from 2.5 to 6.2 μm. This limited sample size is also considered in our numerical modeling for data processing.

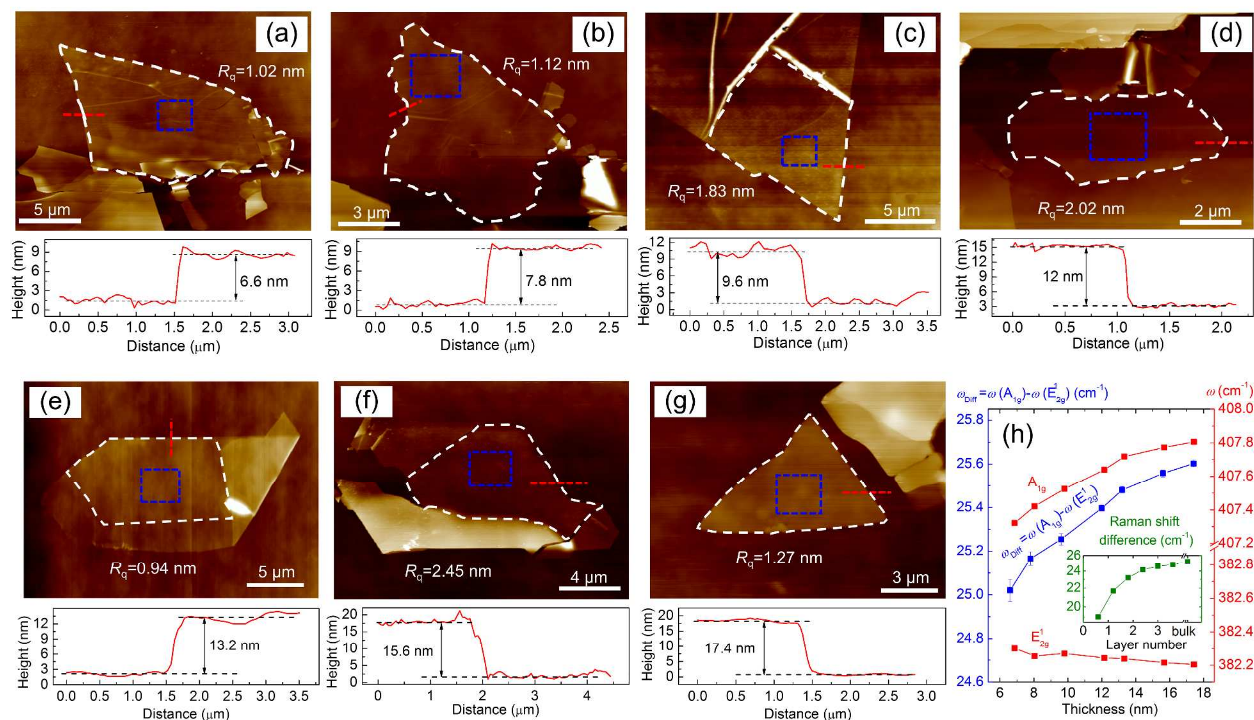

1 2 3 4 5 6 7 8 9 10 11 12 13 14 15 16 17 18 19 20 21 22 23 24 25 26 27 28 29 30 31 32 33 34 35 36 37 38 39 40 41 42 43 44 45 46 47 48 49 50 51 52 53 54 55 56 57 58 59 60

Figure 3. (a)-(g) AFM measurement results of seven MoS_2 samples supported on c-Si. The upper images in (a)-(g) show the AFM images. The white dashed circled area indicates the measured MoS_2 sample. The blue dashed box indicates the sample where the Raman experiment is performed. The height profiles shown below the images correspond to the red dashed lines in the above AFM images. The R_q value in each AFM image indicates the RMS roughness. (h) Thickness dependence of Raman shift of two Raman modes in MoS_2 nanosheets (right vertical axis) and their difference (left vertical axis). The two modes shift away from each other with increased thickness. The inset shows the results and prediction based on Lee *et al.*'s work.[36]

Figure 3 (a)-(g) show AFM images of seven MoS_2 samples supported on c-Si substrate. In each image, we mark the sample area by the dashed white circle. The height profiles shown below the images correspond to the red dashed lines in the AFM images. The samples have a thickness of around 6.6 nm, 7.8 nm, 9.6 nm, 12.0 nm, 13.2 nm, 15.6 nm and 17.4 nm, respectively. The blue dashed square in each sample AFM image shows the area where the laser is focused during different Raman experiments. We also evaluate the sample surface roughness. For example, the 6.6 nm thick sample has a root-mean-square (RMS) roughness (R_q) of 1.02 nm. R_q increases a little bit with increased thickness except for 13.2 nm and 17.4 nm thick sample. These two samples may have fewer wrinkles or ripples. Also, the substrate (c-Si) has a R_q of 0.09 nm which confirms its atomically smooth surface. Figure 3(h) displays the thickness dependence of Raman shift of two Raman modes of MoS_2 nanosheets. The Raman shift of E^1_{2g} mode has a red shift while that of the A_{1g} mode has a blue shift with increased layer number as we found and explained in previous work.[11] The Raman shift difference [$\omega_{\mathrm{Diff}} = \omega(\mathrm{A}_{1g}) - \omega(\mathrm{E}^1_{2g})$] between these two modes is widely used to determine the layer number of MoS_2 nanosheets.[36] So we also

ACS Paragon Plus Environment

1
2
3
4
5
6
7
8
9
10
11
12
13
14
15
16
17
18
19
20
21
22
23
24
25
26
27
28
29
30
31
32
33
34
35
36
37
38
39
40
41
42
43
44
45
46
47
48
49
50
51
52
53
54
55
56
57
58
59
60

plot ω_{Diff} as a function of the sample thickness as blue curve shows, and ω_{Diff} increases with the thickness of MoS_2. Our results agree well with results and predictions of Lee *et al.*'s work.[36]

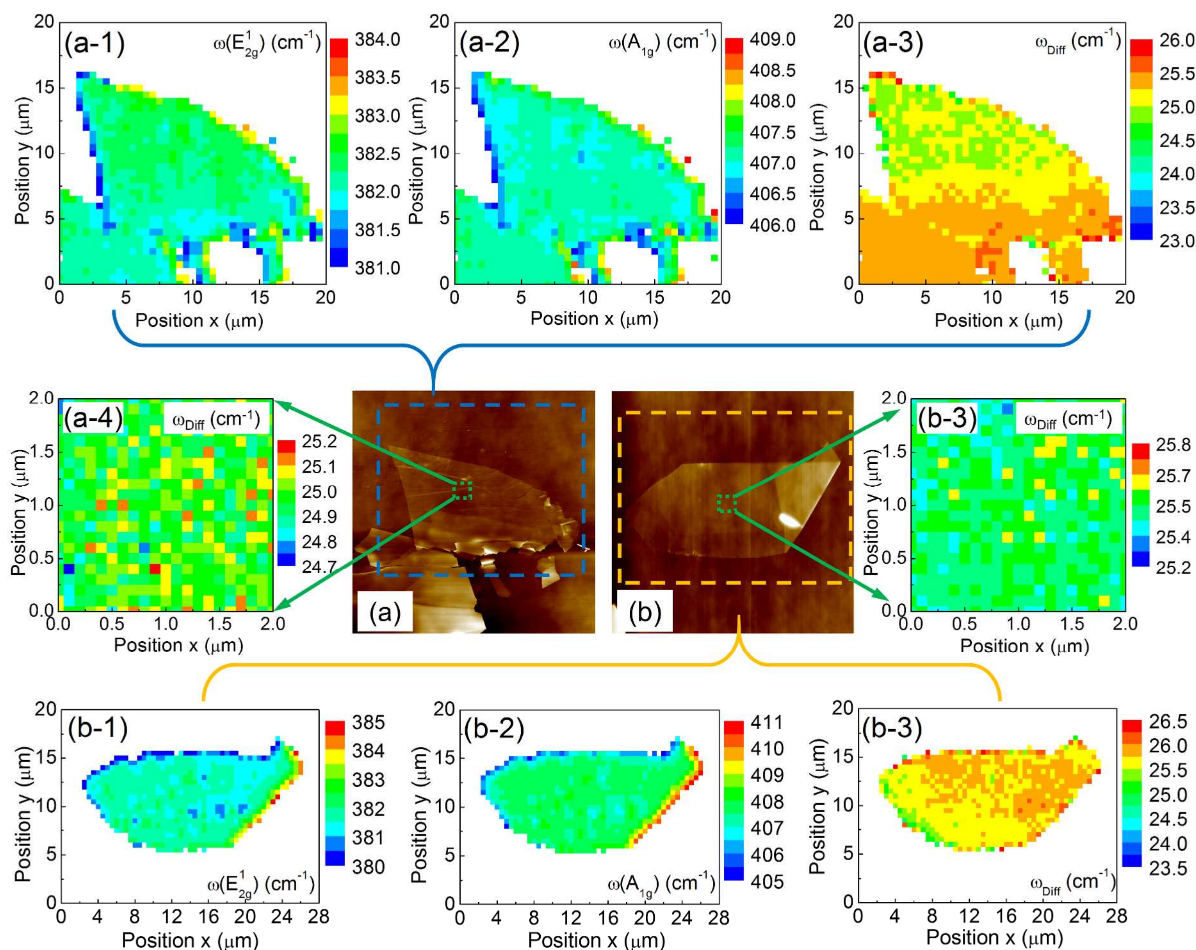

Figure 4. False color images of Raman shift map of 6.6 nm and 13.2 nm thick MoS_2 samples. The blue and yellow dashed squares in the AFM images (a) and (b) mark the area in which the Raman scan was performed as shown in their sub (1)-(3) figures. (a-1) and (b-1) show the Raman shift mapping from E^1_{2g} mode, (a-2) and (b-2) show the Raman shift mapping from A_{1g} mode. The Raman shift difference between these two modes are shown in (a-3) and (b-3). The green dashed squares mark the smaller area for detailed mapping as shown in the (a-4) and (b-4).

1
2
3
4
5
6
7
8
9
10
11
12
13
14
15
16
17
18
19
20
21
22
23
24
25
26
27
28
29
30
31
32
33
34
35
36
37
38
39
40
41
42
43
44
45
46
47
48
49
50
51
52
53
54
55
56
57
58
59
60

The small variance of ω_{Diff} shows that the sample thickness is uniform.

We also perform scanning Raman of 6.6 nm and 13.2 nm thick MoS_2 samples to have a better idea of the uniformity of surface structure. Here we take the 6.6 nm thick MoS_2 sample for example to discuss the scanning results. Figure 4(a) shows its AFM image. The blue dashed square marks the area in which the scanning Raman is performed. The square has a width of 20 μm. Full Raman spectra are recorded for each point with a step size of 500 nm. The spectra are analyzed by an MATLAB-based automatic fitting program, which determines the Raman shift, intensity, and linewidth for two vibration modes of MoS_2 and LO phonon mode of c-Si. We further process the extracted data to create false color images as depicted in Fig. 4(a-1) and (a-2). Here we set Raman shift information of the bare c-Si substrate as white to increase the contrast between sample and substrate. In these figures, we plot the Raman shift of E_{2g}^{1} and A_{1g} modes as a function of position. Figure 4(a-3) shows the Raman shift difference of these two modes. Figure 4(a-4) shows the Raman shift difference from a smaller area as marked with green dashed square in Fig. 4(a). This area is also included in the area where we performed the Raman experiments for D and R determination. The scanning step size for this area is 100 nm. The relatively uniform Raman shift difference mapping shows the sample thickness is uniform and there is no large interface spacing variance.

Thermal response of MoS_2 under picosecond and CW laser heating

In the Raman experiments, for all the seven samples, eight room-temperature Raman spectra are automatically collected at different laser power by the controlled computer to find the laser power coefficient. The CW laser energy is from 1.59 mW to 6.34 mW (0.586 to 2.33 MW/cm^2) under the 100× objective and from 6.03 to 29.2 mW (0.145 to 0.703 MW/cm^2) under the 20×

1
2
3
4
5
6
7
8
9
10
11
12
13
14
15
16
17
18
19
20
21
22
23
24
25
26
27
28
29
30
31
32
33
34
35
36
37
38
39
40
41
42
43
44
45
46
47
48
49
50
51
52
53
54
55
56
57
58
59
60

objective. The ps laser energy is from 1.84 to 6.93 mW (pulse power density is from 0.08 to 0.31 GW/cm^2) under the 50× objective. Note that this laser power is the level just before the laser enters the MoS_2 sample surface. Moreover, the power is maintained as low as possible especially for the ps laser to avoid photon absorption saturation[37-38] and stay within the linear temperature dependence range for Raman properties. For the 532 nm picoseconds pulse laser heating, the saturation intensity is around 1.13 GW/cm^2.[38] When the photon density exceeds that level, the conductance band will be filled and the material will be unable to absorb further photons according to the Pauli-exclusion principles.[39]

Here we also take the 6.6 nm thick sample for example to illustrate the results. Five representative room temperature Raman spectra and their corresponding Lorentzian fits of MoS_2 and Gaussian fits of c-Si under 100× objective by CW laser are shown in Fig. 5 (a) and under 50× objective by ps laser are shown in Fig. 5(b). Also in Fig. 5(a), the inset shows the false color map for the spatial energy distribution of the laser energy beam under 100× objective. The mapping data is from the image captured by a CCD (charge-coupled-device) camera (Olympus DP-26, Olympus Optical Co., Ltd). The corresponding laser spot size (at e^{-1}) on the sample is determined as 0.294 μm. In Fig. 5 (a), both two modes of MoS_2 and LO phonon mode c-Si shift to left (red shift) linearly with increased laser power, and the peak position shifts are visible as $\Delta\omega|(1.59\text{ mW} \sim 6.34\text{ mW})$ by CW laser and $\Delta\omega|(1.84\text{ mW} \sim 4.68\text{ mW})$ by ps laser for MoS_2. The temperature rise of c-Si is not very visible due to its larger thermal conductivity, so the Raman shift changes little. The Raman shift changes indicate that the local temperature of the sample becomes higher under a higher laser power.

1
2
3
4
5
6
7
8
9
10
11
12
13
14
15
16
17
18
19
20
21
22
23
24
25
26
27
28
29
30
31
32
33
34
35
36
37
38
39
40
41
42
43
44
45
46
47
48
49
50
51
52
53
54
55
56
57
58
59
60

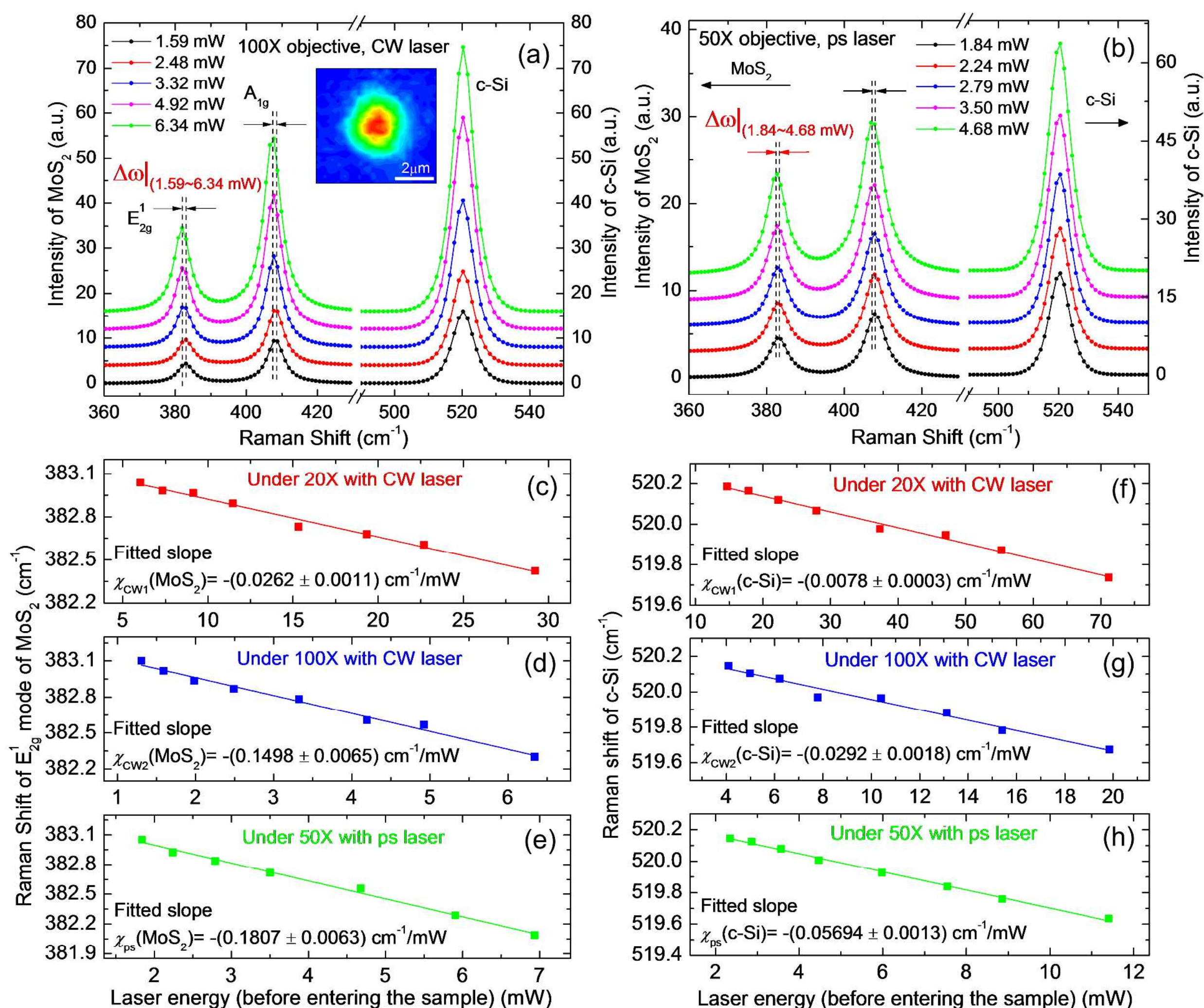

Figure 5. The Raman spectra of MoS_2 nanosheets and the c-Si substrate. The sample with a thickness of 6.6 nm is used as an example to illustrate the ET-Raman experiment results. We use two different objective lenses to generate different laser heating phenomena and different laser sources to generate different energy transport states. The local temperature increases when the laser power increases for both CW laser and ps laser. (a) Five representative Raman spectra of MoS_2 and c-Si at increased excitation laser power under 100× objective with CW laser in the ambient environment. The inset shows the false color map for the spatial energy distribution of the laser energy beam under 100× objective. Here we shift the spectra to increase the clarity for

1
2
3
4
5
6
7
8
9
10
11
12
13
14
15
16
17
18
19
20
21
22
23
24
25
26
27
28
29
30
31
32
33
34
35
36
37
38
39
40
41
42
43
44
45
46
47
48
49
50
51
52
53
54
55
56
57
58
59
60

both (a) and (b). The Raman shifts for two modes of MoS_2 with CW laser are visible as $\Delta\omega|(1.59\text{ mW} \sim 6.34\text{ mW})$ in (a). The temperature rise for c-Si is not very visible because Raman shift changes little due to its large thermal conductivity. With CW laser, the Raman shift for E^1_{2g} mode of MoS_2 and c-Si as a function of laser power under 20× are shown in (c) and (f), and under 100× objective is shown in (d) and (g), respectively. The fitting results (solid lines) for linear power coefficient χ_P are shown in these figures. (b) Five representative Raman spectra of MoS_2 and c-Si at increased excitation laser power under 50× objective with ps laser heating in the ambient environment. The Raman shifts for two modes of MoS_2 vs ps laser power are visible as $\Delta\omega|(1.84\text{ mW} \sim 4.68\text{ mW})$ in (b). The Raman shift for E^1_{2g} mode of MoS_2 and c-Si as a function of laser power under 50× objective with the ps laser power are shown in (e) and (h), respectively.

Two objective lenses with CW laser are used to generate different optical heating phenomena. In our specified laser power range for both CW and ps laser, it is observed that the Raman shift linearly depends on the laser power by $\Delta\omega = \omega(P_2) - \omega(P_1) = \chi(P_2 - P_1) = \chi\Delta P$. χ (cm^{-1}/mW) is the first-order Raman shift power coefficient (RSC) for two vibration modes of MoS_2 and c-Si, and P (mW) is the laser power. In this work, we choose the Raman results from this E^1_{2g} vibration mode to deduce RSC because the in-plane E^1_{2g} mode will be less affected by the interlayer interactions and weakly affected by the substrate.[40] Besides, the E^1_{2g} mode exhibits slightly polar dependence on the laser polarization configuration. So the effects of switching laser sources on Raman results will be eliminated. By CW laser, as shown in Fig. 5(c) and (d), the linear fitting results RSC of MoS_2 E^1_{2g} mode under 20× objective is –(0.026±0.001) cm$^-$

1 2 3 4 5 6 7 8 9 10 11 12 13 14 15 16 17 18 19 20 21 22 23 24 25 26 27 28 29 30 31 32 33 34 35 36 37 38 39 40 41 42 43 44 45 46 47 48 49 50 51 52 53 54 55 56 57 58 59 60

^{1}/mW, and under 100× objective is –(0.150±0.007) cm^{-1}/mW. The RSC value of c-Si, as shown in Fig. 5(f) and (g), under 20× objective is –(0.008±0.001) cm^{-1}/mW, and under 100× objective is –(0.029±0.002) cm^{-1}/mW. The power coefficient under 100× objective (χ_{CW2}) is larger than that under 20× objective (χ_{CW1}). We attribute this to the fact that the temperature rise increases more rapidly under 100× objective due to its higher power density (small laser spot size). Besides, the linear dependence on the laser power for two different heating sizes indicates that there are no significant changes in the thermal properties of materials in our considered laser power range. By ps laser under 50× objective, as shown in Fig. 5(e) and (f), the RSC values of MoS_2 E_{2g}^{1} mode and c-Si are –(0.181±0.006) cm^{-1}/mW and –(0.057±0.001) cm^{-1}/mW, respectively. Also, RSC values for other six samples are summarized in Table S1. The RSC values roughly increase with increased MoS_2 thickness for both CW and ps laser heating. The main reason is that the thicker sample will absorb more energy when the thickness is smaller than its laser absorption depth, so a higher temperature rise will be expected. Under same laser power level (1 mW before it enters the sample), the Raman wavenumber change will increase.

Determination of *D* and *R*

Then a 3D numerical modeling based on the finite volume method is conducted to calculate the temperature rise to determine the hot carrier diffusion coefficient (D) and the interface thermal resistance (R). The modeling setup is shown in Figure. 6(a). (see Materials and Methods section for more details) Specially, τ is set as 1 ns at room temperature.[30] For MoS_2, the photo-excited electrons have a life time of hundreds of picoseconds in few-layered samples and nanoseconds or longer in the thick crystal.[29-30] This effect will be discussed latter in this work. Besides, for phonon contribution to the thermal transport, the material thermal conductivity could be reduced

1
2
3
4
5
6
7
8
9
10
11
12
13
14
15
16
17
18
19
20
21
22
23
24
25
26
27
28
29
30
31
32
33
34
35
36
37
38
39
40
41
42
43
44
45
46
47
48
49
50
51
52
53
54
55
56
57
58
59
60

if the heating size is comparable to, or smaller than the phonon mean free path.[41-42] In this work, for MoS_2, the phonon mean free path is less than 20 nm[43-44] which is much smaller than the laser spot size (radius: 0.294 to 1.15 μm). So the ballistic effect on thermal conductivity is not influential. In this 3D modeling, we only consider the diffusive phonon transport.

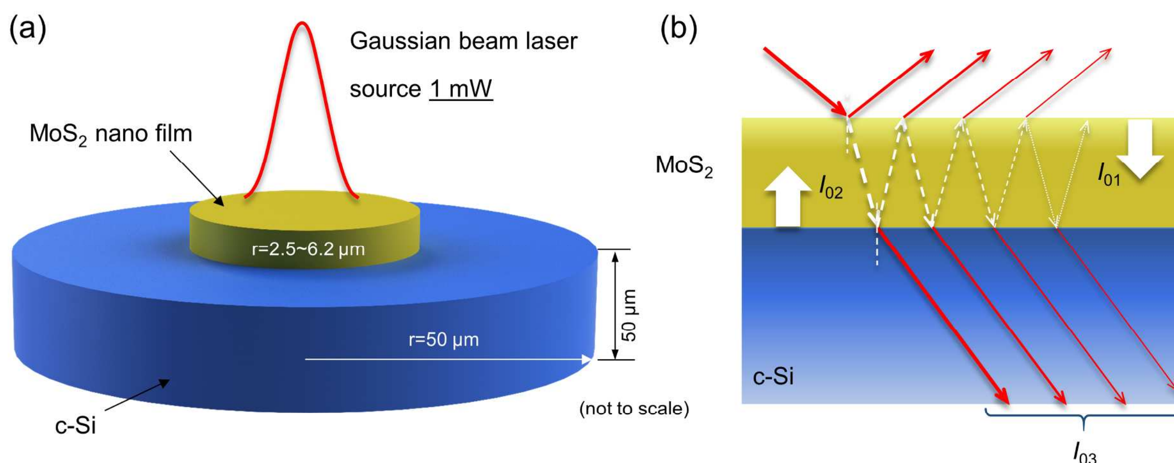

Figure 6. (a) 3D numerical modeling setup. The computational domain of the substrate has a radius and thickness of 50 μm; the MoS_2 sample has the real size. Both CW and ps laser have a Gaussian beam and the same spot size as the experiment. Laser energy is 1 mW before the laser enters the sample surface. (b) When laser beam irradiates the sample surface, multiple reflections happen at the interface between MoS_2 and c-Si. The transmitted power at the top surface (I_{01}), the reflected power at the bottom surface (I_{02}) of MoS_2 and the transmitted power in the c-Si top surface (I_{03}) are calculated out according using the Transfer Matrix Method (TMM).[45]

When a laser beam irradiates the sample surface, multiple reflections happen at the interface between MoS_2 and c-Si as shown in Figure 6(b). Based on the optical properties of these two materials and the Transfer Matrix Method (TMM),[45] we could determine the transmitted power at the top surface (I_{01}), the reflected power at the bottom surface (I_{02}) of MoS_2 and the

1
2
3
4
5
6
7
8
9
10
11
12
13
14
15
16
17
18
19
20
21
22
23
24
25
26
27
28
29
30
31
32
33
34
35
36
37
38
39
40
41
42
43
44
45
46
47
48
49
50
51
52
53
54
55
56
57
58
59
60

transmitted power in c-Si top surface (I_{03}). As mentioned in the introduction section, our method could eliminate the errors from the local laser absorption evaluation and temperature coefficient calibration. The normalized RSC value has no effect of the Raman temperature coefficient, but has conjugated laser absorption effect from MoS_2 and Si. Further data reconstruction is needed to completely rule out the dependence on laser absorption. This is given in Supporting Information S2 with detailed explanations. Take the 6.6 nm thick MoS_2 for example, from the 3D numerical simulation and Raman experiment, we could calculate Θ_1 and Θ_2 for MoS_2 in the (D, R) space. Especially, in the (D, R) space for the zero-transport state, temperature rises for MoS_2 and Si remain constant without changing other parameters. Note in our Raman experiment, as mentioned above, the measured RSC of both MoS_2 and c-Si are Raman-intensity weighted average of the sample. At a location of the sample, the local Raman intensity is proportional to the local laser intensity and the scattered Raman signal multi-reflected in the sample. For the zero-transport state, the measured temperature rise is also time averaged over the pulse width. All these have been considered in our modeling to evaluate the temperature rise of both MoS_2 and c-Si substrate.

Figure 7 (a) and (b) show the calculated normalized RSC mapping for MoS_2. The experimentally obtained normalized RSC (the isolines) could be satisfied by many different (D, R) pairs. In both cases, the lower D or higher R implies a higher normalized RSC value (temperature rise). When D decreases, the heating area will be more confined to the laser heating region that results in a higher local temperature rise and difference. When R increases, under the same temperature drop, less heat could dissipate from MoS_2 to c-Si substrate. Additionally, in Fig. 7 (a) (under 20× objective), the normalized RSC value is less sensitive to the D change. However, this sensitivity increases under 100× objective in Fig. 7 (b). As we discussed in the physical model, when the

ACS Paragon Plus Environment

1 2 3 4 5 6 7 8 9 10 11 12 13 14 15 16 17 18 19 20 21 22 23 24 25 26 27 28 29 30 31 32 33 34 35 36 37 38 39 40 41 42 43 44 45 46 47 48 49 50 51 52 53 54 55 56 57 58 59 60

laser spot size is comparable to, or smaller than the carrier diffusion length, the hot carriers could diffuse out of the heating area more easily and their effect becomes more prominent.

We could determine the exact D and R values by combining the results from these two cases as shown in Fig. 7 (c), the cross point of the blue (Θ_1) and dark red (Θ_2) dashed curves: D is 0.637 cm^2/s and R is 1.75×10^{-7} $K\cdot m^2/W$. As discussed in our previous work,[5] we use the normalized probability distribution function (Ω) to present the final results uncertainty as shown in the false color map of Fig. 7 (c). $\Omega = \exp\left[-(x-\bar{x})^2/(2\sigma^2)\right]$ with x as the variable, $\bar{x}$ as its average, and σ is the standard deviation. In the (D, R) space, we have $\Omega_{(D,R)} = \Omega_{\Theta_1}\cdot\Omega_{\Theta_2}$. The value of $\Omega_{(D,R)} = 0.6065$ corresponding to the σ confidence in the (D, R) space is used to show the final results uncertainty. Finally, the deduced R is $1.75^{+0.08}_{-0.08}\times10^{-7}$ $K\cdot m^2/W$ and D is $0.637^{+0.193}_{-0.154}$ cm^2/s. Also, the final results and the uncertainty for the other six samples are summarized in Table 1 and also plotted in Figure 8 (a) and (b). Our above uncertainty analysis only considers the uncertainty in our characterization. In this work, the in-plane thermal conductivity data of MoS_2 is taken from literatres. We also have conducted analysis to study how sensitive D and R are to the uncertainty carried by k (see section S6 in Supporting Information). We find that R is not sensitive to the uncertainty in k, but D is very sensitive. D decreases by 16.6% if k is increased by 10%. This is understandable since k and D both contribute to in-plane thermal transport. It is conclusive that the heat transfer induced by hot carrier diffusion is less than that by in-plane heat conduction.

1
2
3
4
5
6
7
8
9
10
11
12
13
14
15
16
17
18
19
20
21
22
23
24
25
26
27
28
29
30
31
32
33
34
35
36
37
38
39
40
41
42
43
44
45
46
47
48
49
50
51
52
53
54
55
56
57
58
59
60

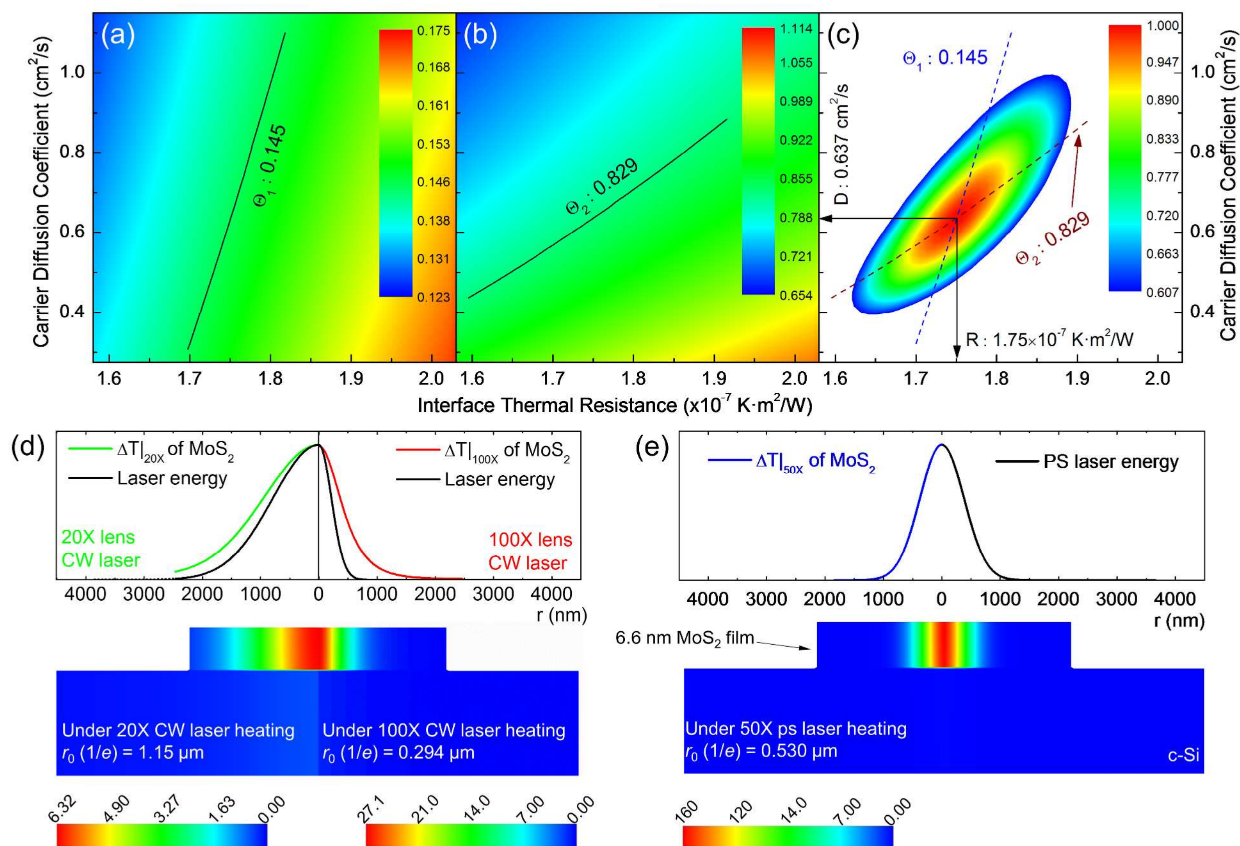

Figure 7. 3D numerical modeling results for the 6.6 nm thick MoS_2 sample to illustrate the temperature distribution. The normalized RSC (Raman shift power coefficient) Θ for different values of *D* and *R* is shown in (a) under the 20× objective and in (b) under 100× objective. The experimentally obtained Θ_1=0.145 and Θ_2=0.829 are shown in these two figures. (c) Determined *D* and *R* as well as the uncertainty region. The normalized probability distribution function (Ω) contour shows the uncertainty distribution: 0.6065 is for the σ confidence. Based on the determined *D* and *R* for this sample, the calculated temperature rise distribution and laser energy distribution in the 6.6 nm MoS_2 sample on c-Si substrate under CW laser heating with 20× and 100× objectives are shown in (d), and under ps laser heating with 50× objective in (e).

1
2
3
4
5
6
7
8
9
10
11
12
13
14
15
16
17
18
19
20
21
22
23
24
25
26
27
28
29
30
31
32
33
34
35
36
37
38
39
40
41
42
43
44
45
46
47
48
49
50
51
52
53
54
55
56
57
58
59
60

Table 1. The summary of the hot carrier diffusion coefficient (D) from the 3D numerical modeling and data fitting, and the corresponding electron mobility (μ) and hot carrier diffusion length (L_D). Also, the calculated the interface thermal resistance (R).

Sample Thickness	D (cm^2/s)	μ (cm^2/V·s)	L_D (μm)	R (10^{-7} K·m^2/W)
6.6 nm	$0.637^{+0.193}_{-0.154}$	$25.5^{+7.71}_{-6.18}$	$0.252^{+0.139}_{-0.124}$	$1.75^{+0.08}_{-0.08}$
7.8 nm	$0.768^{+0.227}_{-0.210}$	$30.7^{+11.1}_{-8.41}$	$0.277^{+0.166}_{-0.145}$	$1.87^{+0.10}_{-0.09}$
9.6 nm	$0.753^{+0.201}_{-0.166}$	$30.1^{+8.04}_{-6.62}$	$0.274^{+0.142}_{-0.129}$	$1.51^{+0.06}_{-0.06}$
12.0 nm	$0.945^{+0.262}_{-0.209}$	$37.8^{+10.5}_{-8.37}$	$0.307^{+0.162}_{-0.145}$	$1.64^{+0.08}_{-0.07}$
13.2 nm	$1.07^{+0.31}_{-0.25}$	$42.7^{+12.6}_{-10.0}$	$0.327^{+0.177}_{-0.158}$	$1.29^{+0.06}_{-0.06}$
15.6 nm	$0.825^{+0.208}_{-0.176}$	$33.0^{+8.34}_{-7.02}$	$0.287^{+0.144}_{-0.132}$	$1.30^{+0.05}_{-0.04}$
17.4 nm	$1.25^{+0.31}_{-0.26}$	$50.0^{+12.5}_{-10.3}$	$0.354^{+0.177}_{-0.161}$	$1.22^{+0.06}_{-0.06}$

To visualize hot carrier diffusion effect on the thermal distribution, we calculate the temperature rise distribution for the 6.6 nm thick MoS_2 sample under CW laser heating with 20× (left part) and 100× (right part) objectives by the determined D and R and show the results in Fig. 7(d). For both cases, the temperature rise is quite uniform in the thickness direction, and the heat conduction along the thickness direction is much larger than that in the in-plane direction in MoS_2 due to its large ratio of lateral size/thickness. Because of the high thermal conductivity of c-Si, the temperature rise of c-Si is very small. Compared with the laser energy distribution (dark curve), the temperature distribution of MoS_2 is out of the laser spot a lot, especially for the small heating size (100× objective). As discussed above, the diffusion length L_D (252 nm for 6.6 nm thick MoS_2) is only 1/5 of r_0 under 20× objective (1.15 μm) and almost same to that under 100×

objective (294 nm). This makes the hot carrier diffusion effect on heat transport more prominent under 100× objective. For the zero-transport state ps laser heating, as shown in Fig. 7(e), the temperature rise of MoS_2 has almost the identical distribution to the ps laser energy distribution. The temperature rise of c-Si is so small due to its large volume and long laser absorption depth (~820 nm). This confirms that the *R* and *D* have negligible effect on the temperature rise of the samples.

As discussed above in the physical model section, during the diffusion process, electrons (*e*) and holes (*h*) move as pairs due to the Coulomb attraction between them. So the measured *D* is the ambipolar diffusion coefficient, $D = 2D_eD_h/(D_e + D_h)$, where $D_{e(h)}$ is the unipolar diffusion coefficient of electrons (holes).[46] However, equal numbers of electrons and holes are generated, and the effective masses of electrons and holes of MoS_2 are comparable and even similar in our optical study.[47] Therefore, both D_e and D_h are assumed to be same. As a result, we can approximately treat the determined *D* in this work as unipolar carrier diffusion coefficients of both electrons and holes. Besides, the diffusion coefficient is related to the mobility (μ) by the Einstein relation in this thermalized system as $D/k_BT = \mu/q$, where k_B, T, and q are the Boltzmann constant, temperature, and the charge of each carrier. Here, we assume that the carriers have a thermal distribution of 300 K during the diffusion process because the energy relaxation time is only several picoseconds.[30] For the 6.6 nm thick MoS_2 nanosheets sample, the measured *D* corresponds to a mobility of μ=25.5 cm^2/Vs. Moreover, 17.4 nm thick MoS_2 has μ=50.0 cm^2/Vs. Our measured μ is very close to the literatures value of 30-60 cm^2/Vs for few-layered MoS_2 on SiO_2,[15] ~70 cm^2/Vs for few-layered MoS_2 on Al_2O_3.[48] One of the biggest difference between the optical and electric methods to study the carrier movement is that we do

not cover the sample (MoS_2 nanosheets) with a dielectric layer such as HfO_2.[34] Nevertheless, our optically measured mobility is still comparable to that measured using the contact methods. As described above, during the diffusion process, the electron-hole pair moves together so that the pair is electrically neutral and will not be influenced by the Coulomb scattering.[20] Hence, our results are much smaller than the theoretical optical-phonon-scattering-limited mobility (~400 cm^2/Vs).[49] Such high mobility could only be approached by adopting high-κ dielectric materials (*e.g.*, HfO_2, Al_2O_3) to build top-gated devices.[34, 50] The dielectric layer is believed to affect (boost) the mobility because of the suppression of Coulomb scattering by the dielectric.[51-52] Besides, it has been shown that some of the reported mobility values may have been greatly overestimated in this top-gated geometry.[53]

Effect of MoS_2 thickness on *R* and *D*

In order to elucidate how R and D values change with MoS_2 thickness, we plot them as a function of MoS_2 thickness as shown in Fig. 8 (a)(b). The detailed results are also summarized in Table 1. Both uncertainties come from the RSC fitting procedure and do not include systematic errors from the uncertainty of P, r_0 and NA. Especially, D has a relatively higher uncertainty than R. In this work, the hot carrier transport is characterized by its effect on thermal energy distribution. To differenitate the R and D effect, we design two steady states with different laser heating sizes. As a result, the hot carrier effect could be very prominent with an ultra small heating size and negligible with very large heating size. Ideally, if we could have two extreme heating states (very large and very small laser spot size), the uncertainty of D could be strongly reduced. In Fig. 8 (b), the carrier diffusion coefficient D is higher for thicker MoS_2 samples. D value almost doubles from 6.6 nm to 17.4 nm MoS_2 sample. A similar trend for this thickness-dependent D value is also found by Li *et al* [54]. This strong dependence may be attributed to

ACS Paragon Plus Environment

1
2
3
4
5
6
7
8
9
10
11
12
13
14
15
16
17
18
19
20
21
22
23
24
25
26
27
28
29
30
31
32
33
34
35
36
37
38
39
40
41
42
43
44
45
46
47
48
49
50
51
52
53
54
55
56
57
58
59
60

weaker in-plane electron-phonon interaction for thicker samples.[55] Besides, the additional MoS_2 layers could serve as a dielectric capping layer which enhances screening of long-range disorder.[15, 54-55] And as the thickness increases, it has also been found that the effect of the charge impurities can be mitigated to some extent which leads to a mobility enhancement.[56]

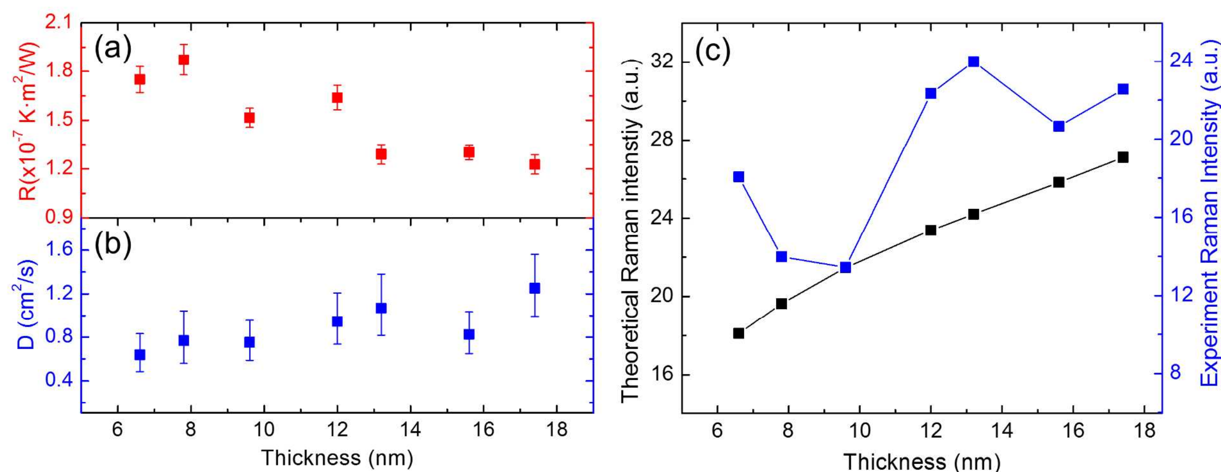

Figure 8. (a) Interface thermal resistance: *R*, (b) hot carrier diffusion coefficient: *D* of seven MoS_2 samples supported on c-Si. (c) The comparison of the experiment Raman peak intensity trend of MoS_2 E^1_{2g} mode and the theoretical Raman intensity *F* for the seven samples.

The interface thermal resistance we obtain here is in the order of 1.5×10^{-7} K·m^2/W. They are larger than what we found in previous work, such as the 8.4 nm MoS_2 on c-Si with *R* is 7.66×10^{-8} K·m^2/W.[11] We attribute this mainly to the unknown errors in laser absorption evaluation and Raman temperature coefficient calibration in our previous work while the ET-Raman completely eliminates the errors from laser absorption evaluation and temperature coefficient calibration. We feel the laser absorption is one of the factors giving the largest uncertainty. First of all, in our previous work and work reported in literatures by other researchers, the laser beam absorption

ACS Paragon Plus Environment

1
2
3
4
5
6
7
8
9
10
11
12
13
14
15
16
17
18
19
20
21
22
23
24
25
26
27
28
29
30
31
32
33
34
35
36
37
38
39
40
41
42
43
44
45
46
47
48
49
50
51
52
53
54
55
56
57
58
59
60

was evaluated based on the refractive index of MoS_2 as 4.4. However, this property features very large deviations from sample to sample, and a broad range of 3.05~5.20 has been reported in literatures.[27-28] Second, a small spacing between the 2D material and the substrate can induce strong optical interference and change the absorption behavior substantially (detailed in the next section). Unfortunately, quantitative knowledge of this spacing is still not available, and this significantly downgrades the measurement accuracy. Third, when calculating laser beam absorption, the laser is assumed normal to the 2D material in past work. In fact, the laser beam is focused with a finite numerical aperture. This could bring in great errors in laser absorption calculation. The smaller R of thicker samples reveals their better interface contact with the substrate, leading to accordingly improved interfacial energy coupling as found in our previous work.[11]

The effect of optical properties

To further elaborate that the optical properties [the complex refractive index (n-ik_L)] of the sample have no effect on the results from ET-Raman technique, we vary the n and k_L values to calculate the laser absorption rate based on TMM as shown in Table S2. In the above 3D numerical simulation, the preset complex refractive index for 6.6 nm MoS_2 is 4.4-1.1i.[27] Based on different combinations of n and k_L values of MoS_2, we calculate the temperature rise ΔT_1 to ΔT_6 and deduce $\Theta(MoS_2)$ [from Eq. (S9) in Supporting Information S2] for both 20× and 100× objectives (two sub-states). $\Theta(MoS_2)$ has a variance of less than one thousandth while changing n or k_L value as shown in Table S2. For example, we reduce n by half and keep k_L value (2.2-1.1i), the calculated $\Theta(MoS_2)$ only increases by 0.11‰. So the change could be neglected. Because the R and D values are determined from $\Theta(MoS_2)$ under 20× and 100× objectives, so it

is conclusive that the ET-Raman technique could eliminate the errors brought in by optical absorption evaluation.

As discussed above, the optical properties of the samples are difficult to accurately determine and vary a lot from sample to sample. Additionally, based on the determined optical properties, the laser absorption rate is estimated assuming a vertical incident laser beam. However, the focused laser beam converges along the propagation direction and this is very complicated to be taken into account when evaluating the laser absorption level. For monolayer MoS_2, the absorbance level experimentally determined varies from 4% to 9%.[57-58] Among the error sources for Raman-based thermal probing technique, the relative error in the laser absorption was by far the dominant contributor. Moreover, the accuracy of the measurement is strongly limited by the uncertainty of the optical absorption evaluation. To this end, some measured the laser absorption level by themselves to consider the absorption variation among samples[59] or discussed the results by referring different absorbance levels obtained from others.[35] All of these treatments still have to consider the effects and errors from optical absorption evaluation so that our results provide the most accurate understanding to date.

The effect of the thickness on interface energy transport: interpretation from interface structure

As we briefed above, the MoS_2-substate interface could have a small spacing, and this spacing will significantly change the laser absorption in MoS_2. This effect has not been considered in the past for laser absorption evaluation. Our ET-Raman technique completely rules out this effect. To have a deeper understanding of this effect, and shed light on above interfacial thermal resistance results, we perform the Raman intensity enhancement study to reveal the interface

1 2 3 4 5 6 7 8 9 10 11 12 13 14 15 16 17 18 19 20 21 22 23 24 25 26 27 28 29 30 31 32 33 34 35 36 37 38 39 40 41 42 43 44 45 46 47 48 49 50 51 52 53 54 55 56 57 58 59 60

structure. As has been investigated, the local interfacial energy coupling will decrease significantly if there is even a tiny spacing (*e.g.* 0.1 nm) at the interface.[11, 24] At the same time, the spacing will induce Raman intensity variation. So in this section we study the Raman intensity of the MoS_2 sample against its thickness, in anticipation to uncover the local interface spacing information.

Figure 8(c) shows the comparison of the experiment Raman peak intensity of MoS_2 E^1_{2g} mode and the theoretical Raman intensity F for our seven MoS_2 samples (see the calculation details for F in the Supporting Information S7). In the comparison, we assume that there is no spacing for 9.6 nm thick MoS_2 sample since it has the lowest theoretical Raman intensity among the seven samples. The deviation of the calculation results from our experiment results confirms the spacing existence for other six MoS_2 samples, especially for the 6.6 nm and 13.2 nm thick ones. This spacing can significantly increase the interface thermal resistance and local laser energy absorption. For the first four samples (6.6 ~ 12.0 nm thick), the 9.6 nm thick sample has the lowest R value due to its perfect interface contact (assumed no spacing). Additionally, the thermal expansion coefficient (TEC) of MoS_2 nanosheets (~10^{-5} K^{-1})[60-61] is larger than that of c-Si (3.9×10^{-6} K^{-1})[62]. Also during the experiment, MoS_2 will have a higher temperature rise than c-Si. So when the sample is under laser heating, these two factors (spacing existence and TEC mismatch) combine to lead to interfacial thermal expansion mismatch between MoS_2 nanosheets and c-Si. This could result in increased local interface spacing, less efficient heat transfer, and a higher interfacial thermal resistance. For the last four samples (12.0 ~17.4 nm thick), the R value has a declining trend. We attribute this to the fact that thicker MoS_2 samples may have smaller TEC value just like PET (polyethylene terephthalate) film.[63] The TEC mismatch between MoS_2 nanosheets and c-Si substrate therefore decreases. As a result, the local interface spacing increase

during experiment will become smaller than the thinner samples, leading to a better interface energy coupling. On the other hand, as we studied before,[11] thicker samples have better mechanical stiffness which could help form a better contact with c-Si substrate during sample preparation. This could also account for the reduced *R* for thicker samples in this work.

Additionally, for some Raman-based thermal probing techniques used in literatures,[35] the TEC mismatch could also introduce large errors in the Raman temperature coefficient calibration. During the laser heating, the temperature rises of two materials are different. Especially, the temperature rise of c-Si is pretty small due to its large thermal conductivity. As a result, the two materials will experience different mechanical stresses. However, during the calibration experiment, they are kept at the same temperature level. Therefore, the thermal expansion mismatch between the two materials are different in calibration and experiment. As a result, the Raman wavenumber changes caused by the stress in MoS_2 during the calibration are very complicated to be examined. Fortunately, as mentioned above, we do not need the Raman temperature calibration results for ET-Raman technique. So this kind of errors could be completely ruled out.

The dependence of hot carrier diffusion coefficient *D* on the carrier lifetime τ

The carrier lifetime τ takes 1 ns in our data processing by solving Eqs. (1) and (2). So the finally determined D is actually dependent on the τ value. To further expound this effect, as we did before,[5] a normalized hot carrier concentration $\xi = \Delta N / \tau$ is defined and used to re-express those equations as (by neglecting the thermal activation term):

$$D\tau\nabla^2\xi - \xi + \Phi\alpha = 0 \, , \tag{5}$$

1 2 3 4 5 6 7 8 9 10 11 12 13 14 15 16 17 18 19 20 21 22 23 24 25 26 27 28 29 30 31 32 33 34 35 36 37 38 39 40 41 42 43 44 45 46 47 48 49 50 51 52 53 54 55 56 57 58 59 60

$$k_T \nabla^2 \Delta T + (h\nu - E_g)\Phi\alpha + E_g \xi = 0 . \tag{6}$$

From these two new equations, term $D\tau$ could be determined without knowing other hot carrier properties. In this work, the carrier diffusion coefficient D is determined based on the carrier lifetime τ. However, the interface thermal resistance R has no dependence on that. The lifetime diffusion length of the hot carriers is evaluated from D and τ as $L_D = \sqrt{\tau D}$. As summarized in Table 1, L_D of seven MoS_2 samples is in the order of 300 nm. Such results are in good agreement with others' work. Wang *et al.* have deduced D around 20 cm^2/s, τ around 0.1 ns, and the corresponding L_D around 450 nm for 1.5~2.2 nm thick MoS_2 on SiO_2/Si measured by spatially and temporally resolved pump-probe technique.[20] Also, Kumar *et al.* have shown that bulk MoS_2 on SiO_2 has L_D around 275 nm with τ around 180 ps measured by a transient absorption microscopy study.[34] We thus firmly conclude that the ET-Raman can securely determine the hot carrier lifetime diffusion length. The diffusion coefficient is dependent on the lifetime data, which needs to be obtained from a separate experiment.

Applicability of ET-Raman technique

This ET-Raman technique could also be applicable for other sample structures, such as suspended 2D material. For this structure, the absorbed laser energy could only dissipate along the in-plane direction. Additionally, the sample thermal relaxation time will be longer and there could be a heat accumulation effect by laser pulses. Therefore, the sample could be easily destroyed during the first several laser pulses. However, by controlling the laser to have a longer cooling time between pulses (low repetition rate), we could still apply ET-Raman to characterize suspended 2D materials. By using two different laser heating sizes in steady state laser heating, and one state in pulsed laser (nanosecond or picosecond laser) heating, both in-plane thermal

conductivity and hot carrier diffusion coefficient could be determined.

We can also use ET-Raman to study other 2D materials, such as TMDs, black phosphorus, and graphene. However, the following points should be paid attention to. First, for materials with an indirect bandgap, like few-layered MoS_2, the radiative recombination of carriers is strongly restricted so that the energy carried by the hot carriers will be transferred to local phonons. For these materials, we could just apply ET-Raman demonstrated in this work to determine their D and R values. Second, for materials with a direct bandgap, such as single-layer MoS_2, the radiative transitions dominate the recombination process. A coefficient may be applied to the last term of Eq. (2) to describe how much energy could transfer to local phonons. Third, for the materials without bandgap, like graphene, no hot electrons are generated during laser excitation. Electrons will carry the photon energy and transfer the energy to local lattice by electron-phonon scattering. So heat conduction equations for both electron and phonon will be needed to describe the diffusion process. Last, under extreme cases, e.g. the material has a very long or very short hot carrier diffusion length compared with the laser heating spot size, the hot carrier diffusion coefficient D will become difficult to measure.

Conclusion

As exemplified by studying the hot carrier diffusion coefficient (D) and the interface thermal resistance (R) of mechanically exfoliated MoS_2 nanosheets on the c-Si substrate, we demonstrate a novel technique: ET-Raman without evaluation of light absorption or absolute temperature rise of MoS_2. The hot carrier effect on heat conduction could significantly extend the heating area, especially when the laser heating size is comparable to the hot carrier diffusion length. The laser focal spot size was varied from 0.294 μm to 1.14 μm to change hot carrier effect in heat

conduction, and the resulting temperature rise effect was measured by power differential of Raman shift. Instead of only using continuous laser, a picosecond pulsed laser was also applied to heat and excite the Raman signal. By studying MoS_2 and the substrate's thermal response under different laser heating states, D and R were determined without knowing the laser absorption or the temperature coefficients of MoS_2. This development successfully eliminates the weak points of currently widely used Raman-based thermal characterization techniques. For our seven MoS_2 samples, under the 1 ns hot carrier lifetime, their hot carrier diffusion coefficient was measured in the order of 1.0 cm^2/s which corresponds to a diffusion length in the order of 300 nm. D was observed to increase with the MoS_2 thickness. This strong dependence may be attributed to weaker in-plane electron-phonon interaction for thicker samples, their enhanced screening of long-range disorder, and improved charge impurities mitigation. No electric field or electrical contacts applied on the sample during this technique assures that the results could reflect the intrinsic properties of 2D materials. R is determined as $1.22\sim1.87\times10^{-7}$ $K\cdot m^2/W$, decreasing with the MoS_2 thickness. This could be caused by the reduced interface spacing increase under laser heating for thicker samples, and the increased stiffness of thicker samples. The local interface spacing was uncovered by comparing the theoretical Raman intensity and experimental data, and was correlated with the observed R variation. To our best knowledge, ET-Raman could also be used for carrier transport and interface energy coupling study of other 2D materials in the most applicable forms with high accuracy and confidence. Such an impactful state-resolved technique opens up a new way for efficient and accurate 2D materials thermal and electrical properties characterization.

Materials and Methods

MoS_2 nanosheets sample preparation

1
2
3
4
5
6
7
8
9
10
11
12
13
14
15
16
17
18
19
20
21
22
23
24
25
26
27
28
29
30
31
32
33
34
35
36
37
38
39
40
41
42
43
44
45
46
47
48
49
50
51
52
53
54
55
56
57
58
59
60

Seven few-layered MoS_2 samples are prepared by the most widely-used micromechanical cleavage technique from their parent bulk MoS_2 crystals (429MS-AB, molybdenum disulfide, small crystals from the USA, SPI Suppliers). Instead of using chemical vapor deposition or liquid exfoliation, we use mechanical exfoliation because it could efficiently produce clean, high quality atomically thin layered structures for their pristine properties and ultimate device performance studies.[64] As in the typical micromechanical exfoliation process, an ordinary adhesive Scotch tape and gel film (Gel-Film, PF-20/1.5-X4, Gel-Pak) are used to prepare layered MoS_2 nanosheets on a freshly cleaned c-Si substrate [*p*-doped, (100)-oriented, 0-100 Ω·cm resistivity, ~335 μm thickness] from University Wafer Company (Boston, MA).[11, 65] The lateral size of layered MoS_2 nanosheets has an equivalent radius ranging from 2.5 to 6.2 μm. We use an optical microscope, atomic force microscope (AFM) (Model MMAFM-2, Digital Instruments, CA, USA) and Raman spectroscopy to identify and locate the MoS_2 nanosheets.

Experimental details

We perform the Raman experiments by using a confocal Raman system that consists of a Raman spectrometer (Voyage™, B&W Tek, Inc.) and a microscope (Olympus BX53). The 532 nm CW laser or ps laser is introduced to the Raman system and the laser power is adjusted by a motorized neutral-density (ND) filter system (CONEX-NSR1 and NSND-5, Newport Corporation). The laser source could be switched by the flip mounted mirror before it enters the Raman system without any other change in the experiment setup. To search for and identify the MoS_2 sample under the microscope, we use a 3D piezo-actuated nano-stage (MAX313D, Thorlabs, Inc.) which has a resolution of ~5 nm. This stage is also used in the following Raman shift scanning experiment and it provides us accurate step size. The laser beam is focused on a specific area of the samples (as shown in Fig.3).

During the experiments, we use LabVIEW-based software to fully control the Raman spectrometer, the motorized ND filter, and 3D nano-stage. The Raman spectrometer could automatically acquire and store the spectrum for each energy level after the ND filter is set or each position after the 3D nano-stage is set during the scanning Raman experiment. This significantly shortens the experiment time, reduces the external disturbance, and therefore improves the precision and accuracy of the experiments. By analyzing the Raman spectrum, we could evaluate the RSC of MoS_2 and c-Si. Based on the RSC under different heating states, we can directly determine the hot carrier diffusion coefficient and interfacial thermal resistance.

3D numerical simulation model

The 3D numerical modeling is based on the finite volume method, we use this to calculate the temperature rise to determine the hot carrier diffusion coefficient (D) and the interface thermal resistance (R). As shown in Figure. 6(a), the computational domain of the substrate has a radius and thickness of 50 μm. The MoS_2 sample is with the actual size and thickness as those in the experiment. The smallest mesh size along the thickness direction is 0.1 nm with an increasing ratio of 1.02 from the MoS_2 surface to the substrate. The smallest mesh size is 1 nm in the radial direction with the same increasing ratio (1.02). In the modeling, the thermal conductivity of MoS_2 in the in-plane and cross-plane directions is taken as $k = 52$ W/m·K[66] and $k_{\perp} = 2$ W/m·K[67], respectively. $k_{c\text{-}Si}$=148 W/m·K is for c-Si.[68] P=1 mW is the excitation laser energy before entering the sample for both CW laser and ps laser sources and the laser spot size is identical to the experiment. For the in-plane thermal conductivity of MoS_2, we also perform the sensitivity study of D and R to it. This could be found in the Supporting Information S6. As considered in our previous work, the MoS_2 nanosheets have the thickness dependent bandgap.[27]

1
2
3
4
5
6
7
8
9
10
11
12
13
14
15
16
17
18
19
20
21
22
23
24
25
26
27
28
29
30
31
32
33
34
35
36
37
38
39
40
41
42
43
44
45
46
47
48
49
50
51
52
53
54
55
56
57
58
59
60

The E_g values for our seven MoS_2 samples are extracted as summarized in Table S1. This consideration, instead of using a constant E_g value, could help us determine R and D values with greater confidence. After the model setup, the carrier diffusion equation [Eq. (1)] is solved and then the heat conduction one with the hot carrier concentration $\Delta N(\mathrm{r}, t)$ used in the source term.

1
2
3
4
5
6
7
8
9
10
11
12
13
14
15
16
17
18
19
20
21
22
23
24
25
26
27
28
29
30
31
32
33
34
35
36
37
38
39
40
41
42
43
44
45
46
47
48
49
50
51
52
53
54
55
56
57
58
59
60

Author Information

Corresponding Author

*E-mail: xwang3@iastate.edu

Present Addresses

271 Applied Science Complex II, Department of Mechanical Engineering, Iowa State University, Ames, IA 50011, USA

Notes

The authors declare no competing financial interest.

ACKNOWLEDGMENTS

Support of this work by National Science Foundation (CBET1235852, CMMI1264399), Department of Energy (DENE0000671, DEEE0007686), and Iowa Energy Center (MG-16-025, OG-17-005) is gratefully acknowledged.

ASSOCIATED CONTENT

Supporting Information

Physical model details for picosecond Raman, data reduction details, ET-Raman experiment results summary, laser pulse accumulation effect from substrate, the effect of optical properties, Sensitivity of *D* and *R* to MoS_2 in-plane thermal conductivity, and the interference induced Raman enhancement.

1
2
3
4
5
6
7
8
9
10
11
12
13
14
15
16
17
18
19
20
21
22
23
24
25
26
27
28
29
30
31
32
33
34
35
36
37
38
39
40
41
42
43
44
45
46
47
48
49
50
51
52
53
54
55
56
57
58
59
60

For Table of Contents (TOC) Graphic Use Only

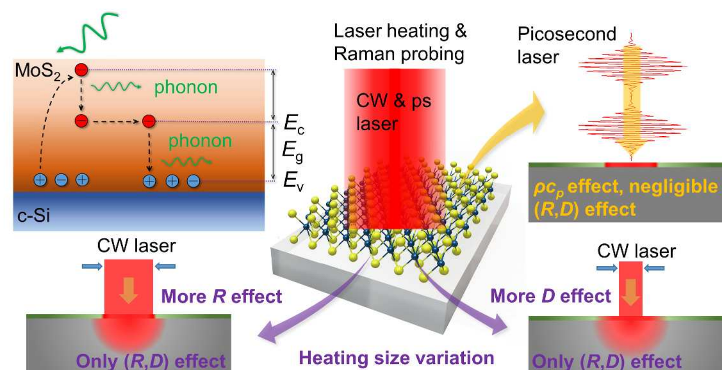

1
2
3
4
5
6
7
8
9
10
11
12
13
14
15
16
17
18
19
20
21
22
23
24
25
26
27
28
29
30
31
32
33
34
35
36
37
38
39
40
41
42
43
44
45
46
47
48
49
50
51
52
53
54
55
56
57
58
59
60

References

1. Pop, E., Energy dissipation and transport in nanoscale devices. *Nano Res.* **2010,** *3* (3), 147-169.
2. Cahill, D. G.; Ford, W. K.; Goodson, K. E.; Mahan, G. D.; Majumdar, A.; Maris, H. J.; Merlin, R.; Phillpot, S. R., Nanoscale thermal transport. *J. Appl. Phys.* **2003,** *93* (2), 793-818.
3. Schulz, M.; Allen, S. T.; Pohl, W. In *The crucial influence of thermal interface material in power electronic design*, Semiconductor Thermal Measurement and Management Symposium (SEMI-THERM), 2013 29th Annual IEEE, IEEE: 2013; pp 251-254.
4. Hopkins, P. E., Thermal transport across solid interfaces with nanoscale imperfections: effects of roughness, disorder, dislocations, and bonding on thermal boundary conductance. *ISRN Mech. Eng.* **2013,** *2013*.
5. Yuan, P.; Liu, J.; Wang, R.; Wang, X., Hot Carrier Diffusion Coefficient of Sub-10 nm Virgin MoS_2: Uncovered by Non-contact Optical Probing. *Nanoscale* **2017,** *9* (20), 6808-6820.
6. Hu, C.; Tam, S. C.; Hsu, F.-C.; Ko, P.-K.; Chan, T.-Y.; Terrill, K. W., Hot-electron-induced MOSFET degradation-model, monitor, and improvement. *IEEE J. Solid-State Circuits* **1985,** *20* (1), 295-305.
7. Sogabe, T.; Nii, K.; Sakamoto, K.; Yamaguchi, K.; Okada, Y., Hot Carrier Transportation Dynamics in InAs/GaAs Quantum Dot Solar Cell. *arXiv preprint arXiv:1702.02015* **2017**.
8. Kim, S.; Konar, A.; Hwang, W.-S.; Lee, J. H.; Lee, J.; Yang, J.; Jung, C.; Kim, H.; Yoo, J.-B.; Choi, J.-Y., High-mobility and low-power thin-film transistors based on multilayer MoS_2 crystals. *Nat. Commun.* **2012,** *3*, 1011.
9. Lee, S.-M.; Cahill, D. G., Influence of interface thermal conductance on the apparent thermal conductivity of thin films. *Microscale Thermophys. Eng.* **1997,** *1* (1), 47-52.
10. Zhu, J.; Tang, D.; Wang, W.; Liu, J.; Holub, K. W.; Yang, R., Ultrafast thermoreflectance techniques for measuring thermal conductivity and interface thermal conductance of thin films. *J. Appl. Phys.* **2010,** *108* (9), 094315.
11. Yuan, P.; Li, C.; Xu, S.; Liu, J.; Wang, X., Interfacial thermal conductance between few to tens of layered-MoS_2 and c-Si: Effect of MoS_2 thickness. *Acta Mater.* **2017,** *122*, 152-165.
12. Wang, T.; Wang, R.; Yuan, P.; Xu, S.; Liu, J.; Wang, X., Interfacial Thermal Conductance between Mechanically Exfoliated Black Phosphorus and SiOx: Effect of Thickness and Temperature. *Adv. Mater. Interfaces* **2017,** *4* (16), 1700233.
13. Liang, Z.; Sasikumar, K.; Keblinski, P., Thermal Transport across a Substrate–Thin-Film Interface: Effects of Film Thickness and Surface Roughness. *Phys. Rev. Lett.* **2014,** *113* (6), 065901.
14. Kazan, M., Interpolation Between the Acoustic Mismatch Model and the Diffuse Mismatch Model for the Interface Thermal Conductance: Application to InN/GaN Superlattice. *J. Heat Transfer* **2011,** *133* (11), 112401-112401-7.
15. Bao, W.; Cai, X.; Kim, D.; Sridhara, K.; Fuhrer, M. S., High mobility ambipolar MoS_2 field-effect transistors: Substrate and dielectric effects. *Appl. Phys. Lett.* **2013,** *102* (4), 042104.
16. Erland, J.; Razbirin, B.; Pantke, K.-H.; Lyssenko, V.; Hvam, J., Exciton diffusion in CdSe. *Phys. Rev. B* **1993,** *47* (7), 3582.
17. Hillmer, H.; Forchel, A.; Tu, C., Enhancement of electron-hole pair mobilities in thin GaAs/Al_xGa_{1-x}As quantum wells. *Phys. Rev. B* **1992,** *45* (3), 1240.

18. Chao, L.-L.; Cargill III, G.; Snoeks, E.; Marshall, T.; Petruzzello, J.; Pashley, M., Diffusion lengths of excited carriers in $Cd_xZn_{1-x}Se$ quantum wells. *Appl. Phys. Lett.* **1999,** *74* (5), 741-743.
19. Ruzicka, B. A.; Wang, S.; Werake, L. K.; Weintrub, B.; Loh, K. P.; Zhao, H., Hot carrier diffusion in graphene. *Phys. Rev. B* **2010,** *82* (19), 195414.
20. Fivaz, R.; Mooser, E., Mobility of charge carriers in semiconducting layer structures. *Phys. Rev.* **1967,** *163* (3), 743.
21. Song, J. C.; Rudner, M. S.; Marcus, C. M.; Levitov, L. S., Hot carrier transport and photocurrent response in graphene. *Nano Lett.* **2011,** *11* (11), 4688-4692.
22. Zhao, X.; Liu, Z.-B.; Yan, W.-B.; Wu, Y.; Zhang, X.-L.; Chen, Y.; Tian, J.-G., Ultrafast carrier dynamics and saturable absorption of solution-processable few-layered graphene oxide. *Appl. Phys. Lett.* **2011,** *98* (12), 121905.
23. Compton, O. C.; Nguyen, S. T., Graphene oxide, highly reduced graphene oxide, and graphene: versatile building blocks for carbon-based materials. *Small* **2010,** *6* (6), 711-723.
24. Tang, X.; Xu, S.; Zhang, J.; Wang, X., Five orders of magnitude reduction in energy coupling across corrugated graphene/substrate interfaces. *ACS Appl. Mater. Interfaces* **2014,** *6* (4), 2809-2818.
25. Cai, W.; Moore, A. L.; Zhu, Y.; Li, X.; Chen, S.; Shi, L.; Ruoff, R. S., Thermal transport in suspended and supported monolayer graphene grown by chemical vapor deposition. *Nano Lett.* **2010,** *10* (5), 1645-1651.
26. Judek, J.; Gertych, A. P.; Świniarski, M.; Łapińska, A.; Dużyńska, A.; Zdrojek, M., High accuracy determination of the thermal properties of supported 2D materials. *Sci. Rep.* **2015,** *5*, 12422.
27. Yim, C.; O'Brien, M.; McEvoy, N.; Winters, S.; Mirza, I.; Lunney, J. G.; Duesberg, G. S., Investigation of the optical properties of MoS_2 thin films using spectroscopic ellipsometry. *Appl. Phys. Lett.* **2014,** *104* (10), 103114.
28. Zhang, H.; Ma, Y.; Wan, Y.; Rong, X.; Xie, Z.; Wang, W.; Dai, L., Measuring the Refractive Index of Highly Crystalline Monolayer MoS_2 with High Confidence. *Sci. Rep.* **2015,** *5*, 8440.
29. Wang, H.; Zhang, C.; Rana, F., Ultrafast dynamics of defect-assisted electron–hole recombination in monolayer MoS_2. *Nano Lett.* **2014,** *15* (1), 339-345.
30. Shi, H.; Yan, R.; Bertolazzi, S.; Brivio, J.; Gao, B.; Kis, A.; Jena, D.; Xing, H. G.; Huang, L., Exciton dynamics in suspended monolayer and few-layer MoS_2 2D crystals. *ACS nano* **2013,** *7* (2), 1072-1080.
31. Nestoros, M.; Forget, B. C.; Christofides, C.; Seas, A., Photothermal reflection versus temperature: Quantitative analysis. *Phys. Rev. B* **1995,** *51* (20), 14115.
32. Christofides, C.; Othonos, A.; Loizidou, E., Influence of temperature and modulation frequency on the thermal activation coupling term in laser photothermal theory. *J. Appl. Phys.* **2002,** *92* (3), 1280-1285.
33. Christofides, C.; Diakonos, F.; Seas, A.; Christou, C.; Nestoros, M.; Mandelis, A., Two-layer model for photomodulated thermoreflectance of semiconductor wafers. *J. Appl. Phys.* **1996,** *80* (3), 1713-1725.
34. Radisavljevic, B.; Radenovic, A.; Brivio, J.; Giacometti, i. V.; Kis, A., Single-layer MoS_2 transistors. *Nat. Nanotechnol.* **2011,** *6* (3), 147-150.
35. Taube, A.; Judek, J.; Łapińska, A.; Zdrojek, M., Temperature-dependent thermal properties of supported MoS_2 monolayers. *ACS Appl. Mater. Interfaces* **2015,** *7* (9), 5061-5065.

1
2
3
4
5
6
7
8
9
10
11
12
13
14
15
16
17
18
19
20
21
22
23
24
25
26
27
28
29
30
31
32
33
34
35
36
37
38
39
40
41
42
43
44
45
46
47
48
49
50
51
52
53
54
55
56
57
58
59
60

36. Lee, C.; Yan, H.; Brus, L. E.; Heinz, T. F.; Hone, J.; Ryu, S., Anomalous lattice vibrations of single-and few-layer MoS_2. *ACS nano* **2010,** *4* (5), 2695-2700.
37. Zhou, K. G.; Zhao, M.; Chang, M. J.; Wang, Q.; Wu, X. Z.; Song, Y.; Zhang, H. L., Size-Dependent Nonlinear Optical Properties of Atomically Thin Transition Metal Dichalcogenide Nanosheets. *Small* **2015,** *11* (6), 694-701.
38. Wang, K.; Feng, Y.; Chang, C.; Zhan, J.; Wang, C.; Zhao, Q.; Coleman, J. N.; Zhang, L.; Blau, W. J.; Wang, J., Broadband ultrafast nonlinear absorption and nonlinear refraction of layered molybdenum dichalcogenide semiconductors. *Nanoscale* **2014,** *6* (18), 10530-10535.
39. Keller, U., Recent developments in compact ultrafast lasers. *Nature* **2003,** *424* (6950), 831-838.
40. Su, L.; Zhang, Y.; Yu, Y.; Cao, L., Dependence of coupling of quasi 2-D MoS_2 with substrates on substrate types, probed by temperature dependent Raman scattering. *Nanoscale* **2014,** *6* (9), 4920-4927.
41. Regner, K. T.; Sellan, D. P.; Su, Z.; Amon, C. H.; McGaughey, A. J.; Malen, J. A., Broadband phonon mean free path contributions to thermal conductivity measured using frequency domain thermoreflectance. *Nat. Commun.* **2013,** *4*, 1640.
42. Hu, Y.; Zeng, L.; Minnich, A. J.; Dresselhaus, M. S.; Chen, G., Spectral mapping of thermal conductivity through nanoscale ballistic transport. *Nat. Nanotechnol.* **2015,** *10* (8), 701-706.
43. Bae, J. J.; Jeong, H. Y.; Han, G. H.; Kim, J.; Kim, H.; Kim, M. S.; Moon, B. H.; Lim, S. C.; Lee, Y. H., Thickness-dependent in-plane thermal conductivity of suspended MoS_2 grown by chemical vapor deposition. *Nanoscale* **2017,** *9* (7), 2541-2547.
44. Cai, Y.; Lan, J.; Zhang, G.; Zhang, Y.-W., Lattice vibrational modes and phonon thermal conductivity of monolayer MoS_2. *Phys. Rev. B* **2014,** *89* (3), 035438.
45. Pérez, E. X., *Design, fabrication and characterization of porous silicon multilayer optical devices*. Universitat Rovira i Virgili: 2008.
46. Neamen, D. A., *Semiconductor physics and devices*. McGraw-Hill Higher Education: 2003.
47. Liu, L.; Kumar, S. B.; Ouyang, Y.; Guo, J., Performance limits of monolayer transition metal dichalcogenide transistors. *IEEE Trans. Electron Devices* **2011,** *58* (9), 3042-3047.
48. Choi, W.; Cho, M. Y.; Konar, A.; Lee, J. H.; Cha, G. B.; Hong, S. C.; Kim, S.; Kim, J.; Jena, D.; Joo, J., High detectivity multilayer MoS_2 phototransistors with spectral response from ultraviolet to infrared. *Adv. Mater.* **2012,** *24* (43), 5832-5836.
49. Kaasbjerg, K.; Thygesen, K. S.; Jacobsen, K. W., Phonon-limited mobility in *n*-type single-layer MoS_2 from first principles. *Phys. Rev. B* **2012,** *85* (11), 115317.
50. Liu, H.; Peide, D. Y., MoS_2 Dual-Gate MOSFET With Atomic-Layer-Deposited Al_2O_3 as Top-Gate Dielectric. *IEEE Electron Device Lett.* **2012,** *33* (4).
51. Ono, M.; Ishihara, T.; Nishiyama, A., Influence of dielectric constant distribution in gate dielectrics on the degradation of electron mobility by remote Coulomb scattering in inversion layers. *IEEE Trans. Electron Devices* **2004,** *51* (5), 736-740.
52. Yang, J.; Xia, Z.; Du, G.; Liu, X.; Han, R.; Kang, J. In *Coulomb Scattering induced mobility degradation in Ultrathin-body SOI MOSFETs with high-k gate stack*, 2006 8th International Conference on Solid-State and Integrated Circuit Technology Proceedings, IEEE: 2006; pp 1315-1317.
53. Fuhrer, M. S.; Hone, J., Measurement of mobility in dual-gated MoS_2 transistors. *Nat. Nanotechnol.* **2013,** *8* (3), 146-147.

54. Li, S.-L.; Wakabayashi, K.; Xu, Y.; Nakaharai, S.; Komatsu, K.; Li, W.-W.; Lin, Y.-F.; Aparecido-Ferreira, A.; Tsukagoshi, K., Thickness-dependent interfacial coulomb scattering in atomically thin field-effect transistors. *Nano Lett.* **2013,** *13* (8), 3546-3552.
55. Lin, M.-W.; Kravchenko, I. I.; Fowlkes, J.; Li, X.; Puretzky, A. A.; Rouleau, C. M.; Geohegan, D. B.; Xiao, K., Thickness-dependent charge transport in few-layer MoS_2 field-effect transistors. *Nanotechnol.* **2016,** *27* (16), 165203.
56. Das, S.; Chen, H.-Y.; Penumatcha, A. V.; Appenzeller, J., High performance multilayer MoS_2 transistors with scandium contacts. *Nano Lett.* **2012,** *13* (1), 100-105.
57. Mak, K. F.; Lee, C.; Hone, J.; Shan, J.; Heinz, T. F., Atomically thin MoS_2: a new direct-gap semiconductor. *Phys. Rev. Lett.* **2010,** *105* (13), 136805.
58. Bernardi, M.; Palummo, M.; Grossman, J. C., Extraordinary sunlight absorption and one nanometer thick photovoltaics using two-dimensional monolayer materials. *Nano Lett.* **2013,** *13* (8), 3664-3670.
59. Zhang, X.; Sun, D.; Li, Y.; Lee, G.-H.; Cui, X.; Chenet, D.; You, Y.; Heinz, T. F.; Hone, J. C., Measurement of lateral and interfacial thermal conductivity of single-and bilayer MoS_2 and $MoSe_2$ using refined optothermal raman technique. *ACS Appl. Mater. Interfaces* **2015,** *7* (46), 25923-25929.
60. El-Mahalawy, S.; Evans, B., The thermal expansion of 2H-MoS_2, 2H-$MoSe_2$ and 2H-WSe_2 between 20 and 800° C. *J. Appl. Crystallogr.* **1976,** *9* (5), 403-406.
61. Gan, C. K.; Liu, Y. Y. F., Direct calculation of the linear thermal expansion coefficients of MoS_2 via symmetry-preserving deformations. *Phys. Rev. B* **2016,** *94* (13), 134303.
62. Touloukian, Y. S.; Powell, R.; Ho, C.; Nicolaou, M. *Thermophysical Properties of Matter-The TPRC Data Series. Volume 10. Thermal Diffusivity*; DTIC Document: 1974.
63. Lin, J.-Y.; Su, F.-I.; Chien, C.-H.; Su, T.-H.; Lin, W.-T.; Jhuang, Y.-D.; Che, J.-W.; Li, J.-J., Thickness Effects on the Thermal Expansion Coefficient of ITO/PET Film. In *Imaging Methods for Novel Materials and Challenging Applications, Volume 3*, Springer: 2013; pp 353-358.
64. Li, H.; Wu, J.; Yin, Z.; Zhang, H., Preparation and applications of mechanically exfoliated single-layer and multilayer MoS_2 and WSe_2 nanosheets. *Acc. Chem. Res.* **2014,** *47* (4), 1067-75.
65. Meitl, M. A.; Zheng-Tao, Z.; Kumar, V.; Lee, K. J.; Xue, F.; Huang, Y. Y.; Adesida, I.; Nuzzo, R. G.; Rogers, J. A., Transfer printing by kinetic control of adhesion to an elastomeric stamp. *Nat. Mater.* **2006,** *5* (1), 33.
66. Sahoo, S.; Gaur, A. P.; Ahmadi, M.; Guinel, M. J.-F.; Katiyar, R. S., Temperature-dependent Raman studies and thermal conductivity of few-layer MoS_2. *J. Phys. Chem. C* **2013,** *117* (17), 9042-9047.
67. Liu, J.; Choi, G.-M.; Cahill, D. G., Measurement of the anisotropic thermal conductivity of molybdenum disulfide by the time-resolved magneto-optic Kerr effect. *J. Appl. Phys.* **2014,** *116* (23), 233107.
68. Neuberger, M., Group IV Semiconducting Materials Composite Data Table. In *Handbook of Electronic Materials*, Springer: 1971; pp 5-5.